IMPACT OF SCALING ON ENERGY DEPOSITION IN SENSITIVE VOLUMES DUE TO DIRECT IONIZATION BY SPACE RADIATION

By

Erik Funkhouser

Thesis

Submitted to the Faculty of the

Graduate School of Vanderbilt University

in partial fulfillment of the requirements

for the degree of

MASTER OF SCIENCE

in

ELECTRICAL ENGINEERING

August, 2014

Nashville, Tennessee

Approved:

Robert Weller, Ph.D.

Robert Reed, Ph.D.

ACKNOWLEDGMENTS

First and foremost I want to thank my family for their support throughout my life. To my parents who have always been extremely supportive of my education and have always encouraged me to follow my passions, wherever they may lead. I am grateful for my older sister who always set the bar high, and was always there to help me walk the trail she had already blazed. I am grateful for my twin brother who has provided companionship throughout my life and has always provided me with a second and unique view of the world.

To the friends and loved ones I have made at all stages in my life. The worries of this world never feel heavy when I am with you. It is comforting to know that I can travel to many places all over the world and feel at home.

I am grateful for the Electrical Engineering faculty for challenging me intellectually. I would like to thank my adviser Robert Weller for the support and guidance he has given over the years. I would also like to thank Robert Reed, Ronald Schrimpf, and Marcus Mendenhall for the many insights they have provided. It has been a privelege to work with such a distinguished group of people.

A special thanks must be given to Makoto Asai, Francesc Salvat, Jose M. Fernandez-Vera, and Josep Sempau for their roles in providing Vanderbilt University with the Monte Carlo transport code PENELOPE 2008. PENELOPE 2008 has played an integral role in this work, much of which would have been impossible without it.

Finally, I would like to thank the Defense Threat Reduction Agency for their support of this work.

TABLE OF CONTENTS

Page

ACKNOWLEDGMENTS . . . . . **i**

LIST OF TABLES . . . . . **iv**

LIST OF FIGURES . . . . . **v**

Chapter

I Introduction **1**

I.1 Space Radiation Environment 2
I.2 Microelectronic Device Scaling 5
I.3 Radiation Effects in Microelectronics 10
I.4 Rate Prediction Techniques 13

II Energy Deposition by Energetic Particles in Material **15**

II.1 Energy Loss by Energetic Particles 15
II.2 Secondary Electron Generation and Physics 16
II.3 Energy Loss Spectrum 21

III Limitations of LET as a Metric for Radiation Effects Analysis **24**

III.1 Ionization Track Structure 24
III.2 Limitation of LET Metric in Small Volumes 29
III.3 Dose Enhancement 32

IV Energy Deposition due to Direct Ionization in Small Volumes **35**

IV.1 Introduction 35
IV.2 Impact of High-Z Material on Direct Ionization Energy Deposition by Ions 40
IV.3 Effect of Energy Loss Straggling in Small Volumes 46

V Conclusions **50**

V.1 Conclusions of the Current Work 50
V.2 Suggestions for Future Work 51

A Concepts and Limitations of mred 53

A.1 Range Cuts 53
A.2 Energy Loss Straggling Limitations 61

BIBLIOGRAPHY 68

LIST OF TABLES

Table Page

I.1 Effect of scaling parameter κ on IC performance [1]. 6

LIST OF FIGURES

Figure		Page
I.1	Integrated flux of proton and electrons in the space environment. Figure (a) shows the integrated flux ($cm^{-2}\,s^{-1}$) of protons with energy greater than 10 MeV in space as a function of earth radii. Figure (b) shows the integrated flux ($cm^{-2}\,s^{-1}$) of electrons with an energy greater than 1 MeV in space as a function of earth radii. The poles of the earth are along the vertical axis [2].	3
I.2	Relative abundance of ion species (up to Z=28) which make up galactic cosmic rays. Heavier elements exist in cosmic rays but in relatively low fluxes [2]	4
I.3	Modulation of GCR flux with solar activity. Strong solar winds dampens the flux of particles originating from outside the solar system [2].	5
I.4	Off state hole density for multiple gate lengths as a function of distance from the oxide/silicon interface in PMOS (a) bulk and (b) Implant Free Quantum Well (IFQW) devices with differing gate lengths. The emergence of a subsurface leakage path in bulk PMOS devices as the gate length decreases can be seen. This leakage path is suppressed in IFQW devices by the quantum well formed due to a SiGe/Si heterojunction [3].	9
I.5	Advanced device structures to suppress off state leakage at gate lengths below 40 nm. Figure (a) shows an ultra-thin-body FDSOI device which suppress off state leakage paths by truncating the channel depth below the gate. Figure (b) shows a finFET device structure which suppresses off state leakage by surrounding the channel with multiple gates providing better electrostatic control. Figure (c) shows an Implant-Free Quantum Well FET which suppress off state leakage by through the use of a heterostructure which confines majority carriers to the gate region.	10
II.1	Electronic and nuclear stopping power for carbon ions of specified energy travelling through silicon. Electronic stopping dominates energy loss by the ion at large energies. Calculations were performed with SRIM.	15

II.2 Time evolution of the spectrum of generated secondary electrons per primary electron with energy 5 keV in silicon. As the primary electron loses energy over time, the spectrum of secondary electrons which it can produce shifts lower in energy. The arrow at 16.7 eV indicates a plasmon peak in silicon. Arrows at higher energies show shell edges of silicon [4]. 18

II.3 Total number of cascading electrons, including those that have stopped, created by an incident electron of energy E_0 as a function of time [4]. . . 19

II.4 Figures (a) and (b) show the inverse mean free path to an elastic and inelastic scattering event respectively for an electron of specified energy. Scattering events alter the direction of motion of an electron limiting their practical range [4]. 20

II.5 Comparison of electron range for different stopping theories. R_{CSDA} denotes the continuous slowing down approximation and R_z denotes the result of Akkerman's Monte Carlo code which takes into account scattering events which limit the practical range of electrons, particularly at low energies [4]. 20

II.6 Relationship between differential and integral spectra, applied in this figure to the recording of the distribution of pulse heights produced by a radiation source interacting with a detector. The spectra portray the same information and are calculable from one another [5]. 22

III.1 Calculated ionization track structure for two sets of ions of the same species and LET but differing energies. In each set, the low energy ion's ionization track structure is more dense than the high energy ion's ionization track structure due to the higher maximum energy of secondary electrons produced by the high energy ions [6]. 25

III.2 Total collected drain current as a function of applied bias for a silicon on sapphire CMOS device exposed to two sets of ions of the same species and LET but differing energy. The collected charge is higher for the high energy ion of each set because the density of generated carriers is lower, leading to less initial recombination and allowing for more of the generated charge to be collected [6]. 25

III.3 Calculation of the generated charge density as a function of distance from the ion track for two ions with similar LETs but very different energies. The generated charge in the inner track, less than approximately 250 nm from the ion track is remarkably similar. Also shown is a Gaussian approximation of generated charge. Gaussian approximations are commonly used in device response simulations [7]. 27

III.4 Boxes show energy deposition in a 50 nm silicon cube at the specified radial distance from the track of a 25 MeV He ion. The bottom of the box shows the average energy deposited and is in good agreement with the Katz model for ionization track structure. The top of the box shows the 90th percentile of energy deposited in the box with the whisker showing the maximum energy deposition event [8]. 29

III.5 The fraction of energy lost by an ion with specified kinetic energy which remains in a sensitive volume with a given average chord length (average distance a secondary electron must go to escape the volume). More energy escapes for smaller volumes (smaller average chord lengths) and higher incident kinetic energies [9]. 30

III.6 Calculation of the fluctuation in energy deposition by isotropic helium of specified velocity in silicon sensitive volumes as a function of the average chord length travelled through that volume. Fluctuations in the deposited energy increase for increasing helium energy and decreasing average chord length of the volume [9]. 31

III.7 Probability density function of the energy lost by 20 MeV protons in silicon of specified thickness. The energy peak at 16.7 eV is a plasmon excitation with higher energy peaks corresponding to shell edges as labled [10]. 32

III.8 Dose profiles at a gold-silicon interface under x-ray and gamma-ray irradiation in the direction specified by the arrow. The equilibrium dose profile is shown by the dotted line [11]. 33

IV.1 Mock up for the target structure used in comparing energy deposition due to direct ionization by protons as calculated by mred+penelope to energy loss calculations for protons performed by Akkerman in [10]. All layers are silicon. The Layers on either side of the sensitive volume are 5 µm thick and provide some amount of charge particle equilibrium. Energy deposition was calculated for sensitive volume thicknesses of 1 µm, 100 nm, and 10 nm. 36

IV.2 Comparison of energy deposition distributions for 20 MeV protons calculated by mred+penelope with energy loss distributions for 20 MeV protons calculated by Akkerman in [10]. The mred target structure used in these calculations is shown in figure IV.1. 39

IV.3 Energy deposition distribution for 100 MeV protons in a 10 nm thick sensitive volume. The peak at 16.7 eV is a plasmon peak. The peak near 100 eV corresponds to the L-shell threshold of silicon. The low energy point occurs due to the continuous energy loss abstraction in GEANT4 and is the minimum amount of energy the proton can lose as it passes through the sensitive volume. The mred target structure for this calculation is shown in figure IV.1. 40

IV.4 Mred target structure used for evaluating the impact of high-Z material on energy deposition in nearby sensitive volumes due to direct ionization by ions. The sensitive volume is 5 nm thick and made of silicon. The BEOL consists of aluminum and SiO_2 as well as two tungsten layers representing vias. The contact is a 19.23 nm layer of tungsten. As a control, the contact layer is switched to silicon. 41

IV.5 Enhancement in the average deposited energy in the sensitive volume due to direct ionization by the specified ion. The mred target structure used in these calculations is shown in figure IV.4. Frontside denotes irradiation incident normal on the BEOL side of the target structure. Backside denotes irradiation incident normal on the wafer side of the target structure. 44

IV.6 Probability of the incident ion depositing the specified amount of energy or more in the sensitive volume. The mred target structure used in these calculations is shown in figure IV.4. 46

IV.7 Mock up of the target structure used for mred+penelope simulations in determining the impact of energy loss straggling on SEU rates in advanced devices. The sensitive volume is a silicon cube 50 nm on a side and is representative of the sensitive volume of a 22 nm SOI SRAM cell. The BEOL consists of aluminum and SiO_2 with two tungsten layers representing vias. A directional flux was used to irradiate the sensitive volume. This flux was contained to the red box which is a square 500 nm to a side and centered on the sensitive volume. 47

IV.8 Integral cross section for energy deposition due to protons in a 22 nm SOI SRAM cell. The estimated critical charge for this technology 0.08 fC which is equivalent to an energy deposition of 1.8 keV. The mred target structure used in these calculations is shown in figure IV.7. 49

A.1 Differential cross section of energy deposition due to direct ionization from 56 GeV Fe in a 5 nm thick silicon sensitive volume with specified range cuts in the sensitive volume. The mred target structure used in these simulations is shown in figure IV.4 with range cuts outside the sensitive volume set to 500 nm except in the tungsten vias where range cuts are set to 10 nm. The data has been scaled by bin width to give an accurate representation of the underlying energy deposition probability distribution. 55

A.2 Effect of range cuts in the contact material on average energy deposition in a neighboring silicon sensitive volume. The mred target structure used in these simulations is shown in figure IV.4. Range cuts in the sensitive volume and the rest of the target structure were set to 500 nm except in the tungsten vias were range cuts were set to 10 nm. In figure A.2a PENELOPE 2008 was used to simulate energy deposition due to electrons. In figure A.2b EmStandardScreened (which uses GEANT4 electrons) was used to simulate energy loss due to ionization. 58

A.3 Effect of range cuts in the sensitive volume on energy deposition due to direct ionization by 56 GeV Fe in a 5 nm thick sensitive volume. The mred target structure used in these simulations is shown in figure IV.1. The target consists of a 5 nm thick sensitive volume with a 5 µm thick layer on both sides of the sensitive volume. The material specifies the material in all layers. Range cuts in the layers surrounding the sensitive volume were set to 500 nm. 60

A.4 Dependence of the differential cross section of energy deposition due to direct ionization by 56 GeV Fe in a 5 nm silicon sensitive volume on range cuts in the sensitive volume. The mred target structure used in these simulations is shown in figure IV.1. The target structure consists of a 5 nm thick sensitive volume with 5 µm thick layer on both sides of the sensitive volume. The material in all layers was silicon. Range cuts in the layers surrounding the sensitive volume were set to 500 nm. . . . 61

A.5 Enhancement of energy deposition in a 5 nm silicon sensitive volume due to nearby tungsten contact for several ions. The mred target structure used in the simulation is shown in figure IV.4 and approximates a modern ultra-thin body FDSOI device. Estimates in the error are based on the variance of the underlying energy deposition distribution. The total number of ions run for each ion species is the same for all energies although the number of ions run differs for different ion species. 63

A.6 Differential cross section of energy deposition due to direct ionization in a 5 nm silicon sensitive volume for 250 MeV u^{-1} and 500 MeV u^{-1} Fe. The mred target structure used in these simulations is shown in figure IV.4 and approximates a modern ultra-thin body FDSOI device. The contact material for these simulations was silicon. The data has been scaled by bin width to give an accurate representation of the underlying energy deposition probability distribution. 65

A.7 Relative energy deposition straggling for 10 MeV protons in silicon for sensitive volumes of specified thickness. The mred target structure used in these simulations is shown in figure IV.1 and consists of a sensitive volume with a 5 µm thick layer of silicon on either side of the sensitive volume to provide some amount of charge particle equilibrium. The results are compared to relative energy loss straggling for 10 MeV protons in silicon as calculated by Akkerman in [10]. 67

A.8 Differential cross section for energy deposition due to direct ionization from 10 MeV protons in 1.1 nm and 2.2 nm silicon sensitive volumes. The mred target structure used in these simulations is shown in figure IV.1 and consists of a sensitive volume with a 5 µm thick layer of silicon on either side of the sensitive volume to provide some amount of charge particle equilibrium. 67

CHAPTER I

Introduction

Electronics in space encounter a harsh radiation environment which affects their performance. Transient effects, termed single-event effects (SEE), stemming from this radiation cause data loss by producing errors in memory, called single-event upset (SEU), and can destroy microelectronic devices outright. Lifetime exposure to radiation leads to performance degradation in what are termed total-ionizing dose (TID) effects. The effects of radiation on microelectronic device operation is a major concern for space missions. Underestimation of the ability of the space radiation environment to wreak havoc on microelectronic device operation has resulted in data loss and, in some cases, the loss of entire satellites.

Since the introduction of the integrated circuit, the desire for higher performance at lower cost has driven microelectronic device scaling. For decades, scaling consisted of shrinking feature sizes while the overall structure of microelectronic devices remained primarily the same. The effect scaling has had on the radiation response of microelectronics is mixed. Thinner gate oxides have drastically reduced the impact of TID; however, reductions in the amount of charge controlling a logic state have made devices more susceptible to SEU.

To push scaling into the deep sub-micron region, changes to the microelectronic device structure were required. This included the introduction of new materials and changes to the device structure in order to obtain tight confinement of channel regions. These changes present challenges to conventional error rate analysis as an underlying assumption that energy deposition in a sensitive volume by an ion is well characterized by the ion's linear energy transfer (LET) may not be valid. The use of different materials near sensitive volumes introduces the possibility that energy deposition in the sensitive volume will be deviate from that expected in an equilibrium case due to non-local deposition of energy

lost by an ion. This phenomenon has already been observed for x-ray and gamma-ray sources [11, 12]. Furthermore, the increase in the variance of the energy loss distribution, termed energy loss straggling, in small volumes limits the ability of LET to accurately describe energy deposition by ions in small sensitive volumes. This is particularly problematic for light ions for which the energy loss straggling in small volumes can exceed the LET [10].

This work seeks to use the mred Monte Carlo tool to explore the realistic impact that changes in microelectronic device structure due to scaling have on energy deposition due to direct ionization by ions found in the space environment. The results suggest that the use of high-Z materials near sensitive device regions does not have a meaningful impact on the radiation response of highly scaled microelectronic devices. However, exploration of SEU induced by protons in a target structure representative of a 22 nm SOI SRAM cell shows that energy loss straggling may play a meaningful role in determining the SEU cross section for advanced devices. This is due to the observation of protons with an LET well below the critical LET depositing energy well above that required to induce SEU. The implications of this result on error rate analysis for highly scaled devices is discussed.

I.1 Space Radiation Environment

The radiation environment encountered by a satellite is highly dependent on its orbit's altitude and inclination. While the Earth's magnetic field provides some protection from galactic cosmic rays, it also traps protons and electrons. These trapped protons and electrons form radiation belts commonly referred to as Van Allen Belts [13]. The inner Van Allen Belt is dominated by high energy protons which can have energies in the hundreds of MeV. The outer Van Allen Belt is dominated by electrons which exist at higher fluxes but at a lower energies than in the inner belt. Electrons reach a maximum of about 10MeV in the inner Van Allen belt but reach a maximum of only 7MeV in the outer Van Allen belt [2]. Proton and electron fluxes as a function of distance from the Earth are shown in I.1.

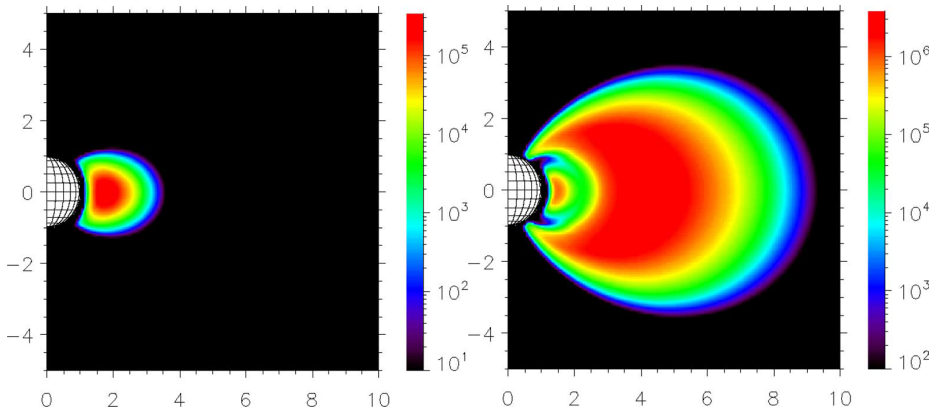

(a) Proton Flux

(b) Electron Flux

Figure I.1: Integrated flux of proton and electrons in the space environment. Figure (a) shows the integrated flux ($cm^{-2}\,s^{-1}$) of protons with energy greater than 10 MeV in space as a function of earth radii. Figure (b) shows the integrated flux ($cm^{-2}\,s^{-1}$) of electrons with an energy greater than 1 MeV in space as a function of earth radii. The poles of the earth are along the vertical axis [2].

The inclination of orbit also dramatically affects the radiation environment encountered. The Earth's magnetic field is dipolar and converges near the geographic pole of the earth, leading to a sparseness of the magnetic field in these regions. Satellites operating in polar orbits, therefore, are less protected from galactic cosmic rays and experience more severe proton and electron environments than would be encountered in a similar equatorial orbit [2, 13, 14]. Valuable orbits, such as those over the South Atlantic, must contend with these radiation environments. The relatively harsh environment over the South Atlantic is termed the South Atlantic Anomaly and occurs due to the off axis nature of the Magnetic Pole which leads to a sparseness of the field over the South Atlantic. This allows the inner Van Allen belt to dip down leading to relatively high low earth orbit proton fluxes in this region [13].

Beyond the trapped radiation belts, satellites escape trapped proton and electrons but are subjected to the full background cosmic ray flux. Valuable orbits such as Geosynchronous (geo) operate in this environment. Cosmic rays originating from outside our solar system (galactic cosmic rays) are generally believed to be super novae remnants. All elements

through uranium are contained in galactic cosmic rays (GCR), but the flux of elements heavier than iron falls off quickly. The relative abundance of ions contained in cosmic rays is given in I.2. GCR can have energies up 10^{11}GeV; however, GCR fluxes peak at ion velocities around $1\text{GeV}\,\text{u}^{-1}$ [2].

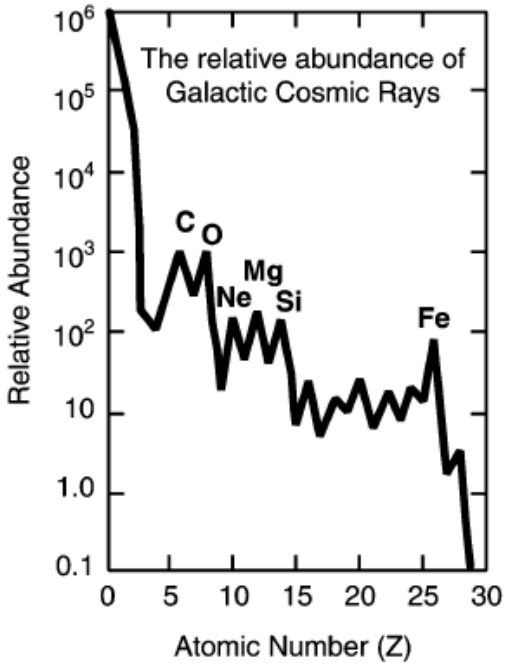

Figure I.2: Relative abundance of ion species (up to Z=28) which make up galactic cosmic rays. Heavier elements exist in cosmic rays but in relatively low fluxes [2]

While the space radiation environment has been generally described, it is important to note that the space radiation environment is highly variable. Trapped proton and electron fluxes are highly dependent on solar activity and can be significantly altered by manmade sources such as the detonation of a nuclear weapon in the upper atmosphere. Solar activity dampens GCR fluxes which peak during solar quite periods as shown in I.3. However, solar activity, while proton and electron rich, ejects all elements through uranium [2, 13].

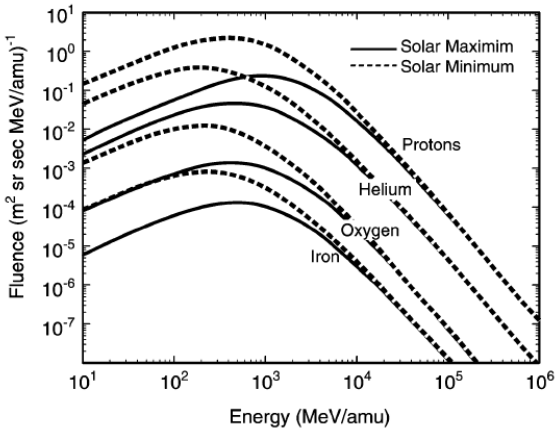

Figure I.3: Modulation of GCR flux with solar activity. Strong solar winds dampens the flux of particles originating from outside the solar system [2].

I.2 Microelectronic Device Scaling

The beginning of the microelectronics industry can be traced back the filing of a patent in 1925 by Polish physicist J.E. Lilienfeld which described a field effect transistor. However, the first field effect transistor was made at Bell labs in 1947 by John Bardeen, Walter Brattain, and William Shockley. Most early work in the industry, including the production of the first integrated circuit, was done using germanium as the semiconductor material. However, germanium's native oxide is soluble in water and a high-quality low-defect germanium/germanium oxide interface is difficult to grow. This led to germanium's replacement with silicon, because silicon readily forms a high quality oxide in the form of SiO_2 [3]. Since the 1960s, silicon has dominated the semiconductor industry, and while many have proclaimed the death of silicon due to scaling, device concepts exist which would continue the use of silicon to the 5nm node [15].

Almost immediately following the development of the integrated circuit, Gordon Moore made his famous prediction that the number of transistors per unit area of an IC would double every two years. The driving force behind Moore's law is the benefits of device scaling. Ideally, structural parameters and operating voltages would be scaled in concert so that field internal strengths do not change. This type of scaling is referred to as constant

Parameter	Constant Field Scaling	Constant Voltage Scaling
Dimensions	$\frac{1}{\kappa}$	$\frac{1}{\kappa}$
V_{DD}	$\frac{1}{\kappa}$	1
Fields	1	κ
V_T	$\frac{1}{\kappa}$	1
Current	$\frac{1}{\kappa}$	κ
Capacitances	$\frac{1}{\kappa}$	$\frac{1}{\kappa}$
Delay Time	$\frac{1}{\kappa}$	$\frac{1}{\kappa^2}$
Power/Circuit	$\frac{1}{\kappa^2}$	κ
Power x Delay	$\frac{1}{\kappa^3}$	$\frac{1}{\kappa}$
Power/Area	1	κ^3
Line Resistance	κ	κ
RC	1	1
IR/V_{DD}	κ	κ^2

Table I.1: Effect of scaling parameter κ on IC performance [1].

field scaling and results in not only in an increase in the number of transistors per unit area but also an increase in the speed of the IC for no additional power as well as a reduced cost per function. However, system limitations on operating voltage often led to scaling of device parameters without a corresponding decrease in operating voltage. This is referred as constant voltage scaling and results in results in greater speed increases than constant field scaling although at a power cost. Furthermore, performance gains from constant field scaling can be limited due to velocity saturation of carriers. The ideal scaling benefits for constant field scaling and constant voltage scaling are shown in table I.1. From the 1970s to the early 2000s, the actual structure of the MOSFET remained little changed despite a massive decrease in minimum feature size [1].

Around 2000, several performance issues began to force changes to materials used in microelectronic devices to continue scaling trends. Leakage current due to tunneling presents a limit to how thin of an oxide can be used. In order to continue scaling, SiO_2

was replaced with high-κ dielectrics such as HfO_2, ZrO_2, and Al_2O_3 [16]. As gate capacitance continued to drop with each generation, poly depletion became a serious issue. The depletion depth in a polysilicon gate is given as $W_{poly} = \frac{\varepsilon_{ox} V_{ox}}{t_{ox} q N_{poly}}$ where V_{ox} is the voltage drop over the oxide. Practically, doping levels in silicon are limited to $10^{20}cm^3$, and the supply voltage for each generation is generally fixed. This means that the poly depletion region grows with each generation. Furthermore, this depletion region has a capacitance associated with it. As the gate capacitance decreases due to a thinner oxide or high-κ oxide, the capacitance of the poly depletion region becomes non negligable and adds in series to the gate capacitance giving a total capacitance of $C = (\frac{t_{ox}}{\varepsilon_{ox}} + \frac{W_{poly}}{\varepsilon_{Si}})^{-1}$. This has a severe effect on device performance and introduces skew in transistor VC characteristics as the depletion region depth in the poly gate is non-constant for applied gate voltage.

To solve the problem of poly depletion, metal gates were introduced. Metal gates pose their own challenges as the metal must be selected in conjunction with the oxide used so that a work function which allows for the proper threshold voltage is obtained [17]. Furthermore, the metal must survive high temperature processing steps limiting choices primarily to refractory metals and their silicide. Metals commonly used in gate stacks include Ta, TaN, TiN, Ni, Co, Pt, Mo, Sn, and W [18–23]. Molybdenum and tungsten are of particular interest, because the work function of molybdenum can be controlled with nitrogen implantation and tungsten's work function is midgap, meaning either of these metals could be used to provide a process with a single type of metal gate for both PMOS and NMOS devices, reducing process complexity. Source and drain contacts are also now typically silicide and/or metal clad in order to reduce their parasitic series resistance. In order to maintain good transconductance and device performance, the parasitic series resistance of a device must be a small fraction of the on resistance which reduces with scaling [24].

As devices have continued to scale, short channel effects have limited the gate's control of the channel. This allows the formation of a sub-surface leakage path which increases off state current. This can be seen in figure I.4a which shows TCAD simulations of off state

hole density of a bulk silicon PFET as a function of depth from the gate. Several strategies which fundamentally alter the microelectronic device structure are being explored in order to regain control of the channel. The most common is a dual gate FET. It is common to implement the dual gate by growing a silicon channel on the substrate plane and surrounding this channel by a gate. This devices structure is shown in figure I.5b and is generally referred to as a finFET. Currently, Intel uses finFETs in commercial processors [25]. A second method of controlling the channel which would preserve the planar structure of microelectronic devices is Ultra-Thin Body Fully-Depleted Silicon on Insulator (UTBB FD-SOI). In this method, raised source drain and an ultra-thin body (less than 10 nm) allows the gate to suppress off state leakage. The structure of UTB FD-SOI is shown in figure I.5a. This technology is commercially available in the ARM Cortex^{TM}-A9 which is a 28 nm technology with a body depth of 7 nm [26]. Other blue sky technologies are also being developed to control off state leakage. One promising technology is the Implant-Free Quantum Well Field Effect Transistor (IFQW FET). The PFET implementation of the IFQW FET utilizes a SiGe/Si heterojunction which confines majority carriers to the gate region, suppressing the subsurface off state leakage path. This can be seen in figure I.4b which shows off state hole density for an IFQW PFET as a function of distance from the gate. The structure of an IFQW PFET can be seen in figure I.5c.

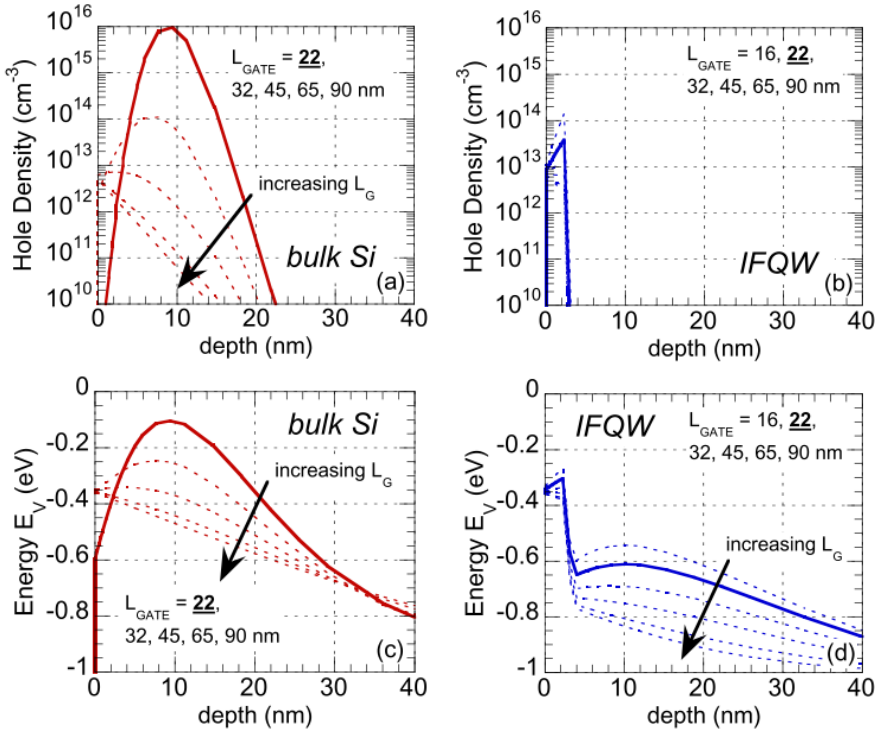

(a) Bulk Silicon PFET

(b) IFQW PFET

Figure I.4: Off state hole density for multiple gate lengths as a function of distance from the oxide/silicon interface in PMOS (a) bulk and (b) Implant Free Quantum Well (IFQW) devices with differing gate lengths. The emergence of a subsurface leakage path in bulk PMOS devices as the gate length decreases can be seen. This leakage path is suppressed in IFQW devices by the quantum well formed due to a SiGe/Si heterojunction [3].

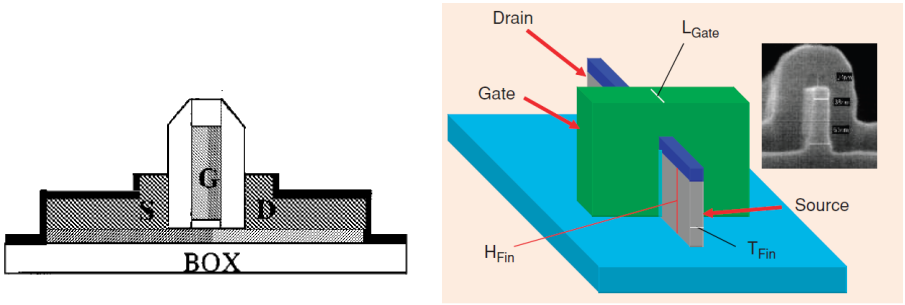

(a) UTB FDSOI [27]

(b) finFET [28]

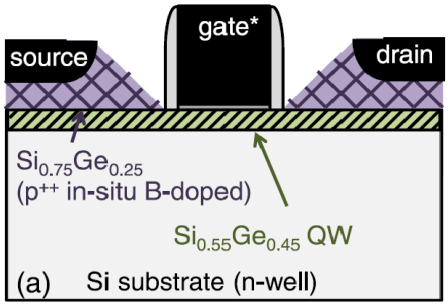

(c) IFQW FET [3]

Figure I.5: Advanced device structures to suppress off state leakage at gate lengths below 40 nm. Figure (a) shows an ultra-thin-body FDSOI device which suppress off state leakage paths by truncating the channel depth below the gate. Figure (b) shows a finFET device structure which suppresses off state leakage by surrounding the channel with multiple gates providing better electrostatic control. Figure (c) shows an Implant-Free Quantum Well FET which suppress off state leakage by through the use of a heterostructure which confines majority carriers to the gate region.

I.3 Radiation Effects in Microelectronics

The root cause of all radiation effects in microelectronics is the transfer of energy from radiation to the material which makes up the microelectronic device. The processes by which energetic particles lose energy in a medium are discussed in detail in Chapter 2. For many applications, it is sufficient to simply describe the average energy lost by a particle per unit distance it travels in a material. This is termed the particle's stopping power and denoted $\frac{dE}{dx}$. A particle's linear energy transfer (LET) is a more restrictive term for energy loss and is rigorously defined as the average energy lost per unit length travelled by a parti-

cle excluding all generated secondary electrons with initial kinetic energy above an energy E_0 [9]; however, the terms LET and stopping power are commonly used interchangeably as it assumed, unless otherwise stated, that E_0 is taken at ∞ in which case the LET and the electronic stopping power of a particle are identical. In the radiation effects community, the term LET is commonly used to describe energy loss by a particle per unit length it travels in a material and is commonly normalized by the material density as $LET = \frac{1}{\rho}\frac{dE}{dx}$ (where ρ is the material density). LET is typically given in units of $\frac{\text{MeV}-\text{cm}^2}{\text{mg}}$.

The energy deposited by a particle as it passes through a material leads to the generation of electron hole pairs. If this occurs in a depletion region in a microelectronic device, the electron hole pairs will separate. This leads to a current transient which affects the output potential and is known as a single event transient (SET). If this transient changes the state of a memory element, it is known as a single event error (SEE) or single event upset (SEU). The minimum amount of charge which must be collected at a circuit node to cause an SEU is known as the critical charge Q_{crit} [29]. The volume of a device from which this charge can be collected is termed a sensitive volume. In bulk devices, this sensitive volume extends considerably further than the depletion region width. This is due to an extension of the electric fields contained in the depletion region along the particle track in a process known as field funneling [30]. In SOI devices, the collection depth is limited to the body depth by the buried oxide. However, charge collection in SOI devices can be complicated by bipolar amplification. Bipolar amplification is a floating body effect which leads to the injection of carriers, exacerbating the effect of the charge deposited by an ion. Bipolar amplification can be limited by the use of body ties [31].

The cumulative energy deposited by radiation passing through a material over its lifetime can affect its performance in what are known as total ionizing dose (TID) effects. Electron hole pairs generated in the oxide of a device are quickly separated by the electric field across the oxide. In silicon dioxide, electrons are swept out of the oxide within a picosecond, but holes are relatively immobile, becoming trapped. This trapped positive

charge causes a negative threshold voltage shift of the device. Over time scales of hours, days, and even years, trapped holes transport out of the device oxide leading to a recovery of the threshold voltage. As holes transport out of the oxide, they free trapped hydrogen. If this free hydrogen transports to the Si/SiO_2 interface, it can interact with a Si-H bond, forming H_2 and leaving behind a dangling bond. These dangling bonds are known as P_b centers and make up the bulk of interface traps. P_b centers are amphoteric, becoming donor like when the Fermi level is below mid-gap, neutral when the Fermi level is at mid-gap, and acceptor like when the Fermi level is above mid-gap [32]. The charging and discharging of these traps stretches out the I_d vs V_{gs} characteristics of a device and can cause parametric failure of a circuit.

As devices have scaled, TID effects in gate oxides have been largely mitigated by the reduced gate oxide thickness t_{ox}. The reduction in the volume of oxide leads to a reduction in the number of trapped holes at a given dose, and, therefore, the threshold voltage shift due to trapped holes scales with t_{ox}^2, and the buildup of interface scales traps with t_{ox} [33]. As a result, the primary cause of TID induced performance degradation in modern devices is TID effects in isolation oxides. Trapped charge and the buildup of interface traps in isolation oxides can cause the formation of a leakage path between devices separated by the isolation oxide. TID susceptibility of SOI devices is typically much worse than their bulk counterparts due to the presence of the buried oxide (BOX). Even in modern processes, the BOX tends to be thicker than 100 nm. In SOI technology, the BOX/Si interface effectively forms a back gate which is electrically coupled to the front gate. Trapped charge in the BOX and interface trap buildup at the BOX/Si interface can then alter the device performance in much the same way as it would if it were in the front gate oxide.

An overview of SEU and TID effects have been presented; however, it should be noted that there are peculiarities within these topics such as enhanced low dose rate sensitivity (ELDRS) which will not be discussed in detail. There is also a myriad of other radiation induced effects in microelectronics which will not be discussed in detail. These include

destructive effects such as latch-up, single event gate rupture (SEGR), and single event burn out.

I.4 Rate Prediction Techniques

Conventionally, SEU rate prediction has been performed using the rectangular parallelepiped chord length model (RPP model). This method defines a rectangular parallelepiped sensitive volume from which charge can be collected. The volume typically represents one bit with the chip response assumed to be the response of an aggregate of the sensitive volumes. By defining a critical energy E_c which must be deposited in order to generate the critical charge Q_c to upset the cell, one can integrate over all ions in the environment with an LET and path length which leads to the deposition of energy greater than E_c to find an error rate. This is expressed in the equation $R(E_c) = A_p \int_{s_{min}}^{s_{max}} \Phi(L_t(s,E_c)) f(s) ds$ where A_p is the average projected area of the RPP, $s_{min} = 0$ (the minimum chord length through the RPP), $s_{max} = (x^2 + y^2 + z^2)^{1/2}$ (the maximum chord length through the RPP), $\Phi(L_t(s,E_c))$ is the flux of particles whose LET is such that more than E_c will be deposited over a chord length s in the RPP, and $f(s)$ is the probability density of a chord of length s in the RPP [34]. This integral requires a description of the radiation environment and is typically performed using codes such as CREME96 [35].

Despite much success, many of the fundamental assumptions in the RPP model have been called into questions. This has spurred the development of Monte Carlo error rate prediction techniques which have been successful in explaining cases in which the RPP failed catastrophically to predict on orbit error rates [36]. The Monte Carlo simulation tool developed by Vanderbilt University and used to in the work presented in this thesis is named mred (Monte Carlo Radiative Energy Deposition). At the tool's core is the GEANT4 C++ toolkits. GEANT4 is a collection of object oriented radiation transport codes written and maintained by an international collaboration. The toolkit attempts to incorporate all known physics relating to particle interactions and allows the definition of complex targets [37].

Mred uses the programming language Python as an interface to the GEANT4 toolkit. This is achieved by wrapping the GEANT4 source code with the help of SWIG [38]. Mred also offers several extensions to the standard GEANT4 physics library [39]. The extension most relevant to this work is the incorporation of PENELOPE 2008 [40]. PENELOPE 2008 is a Monte Carlo code which deals specifically with electron and positron transport in matter and is capable of accurately tracking electrons down to 50 eV

CHAPTER II

Energy Deposition by Energetic Particles in Material

II.1 Energy Loss by Energetic Particles

The average rate of energy lost by a particle as it travels through a material is termed the particle's stopping power and denoted $\frac{dE}{dx}$. The stopping power of charged particles can further be separated into electronic stopping power and nuclear stopping power. As the names imply, the electronic stopping power is energy loss due to coulombic interactions with the electron cloud of the target material while the nuclear stopping power is energy loss due to coulombic interactions with the nuclei of the target material. It is possible to make this distinction because perturbation of the electron cloud occurs on a much faster time scale than the recoiling of struck nuclei. The electronic stopping power dominates energy loss for energetic charged particles, with nuclear stopping power becoming relevant only as the particle nears stopping The relative importance of electronic and nuclear stopping power for carbon travelling in silicon as its energy changes is shown in figure II.1.

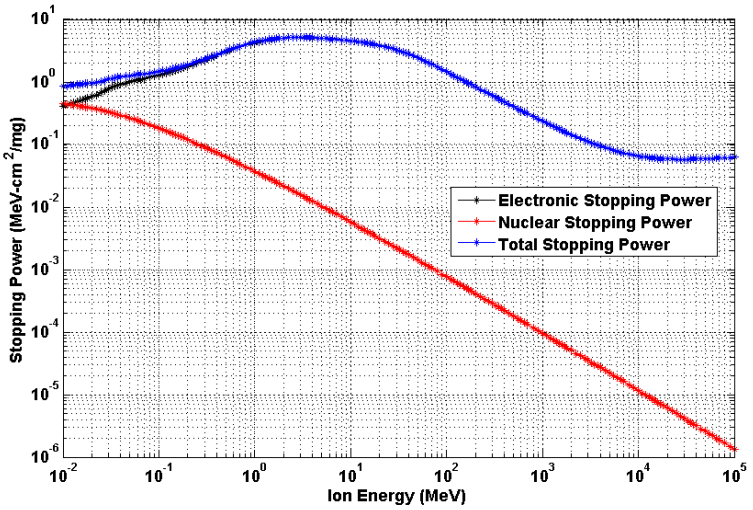

Figure II.1: Electronic and nuclear stopping power for carbon ions of specified energy travelling through silicon. Electronic stopping dominates energy loss by the ion at large energies. Calculations were performed with SRIM.

It is also possible for a particle to lose energy through non-coulombic interactions with target nuclei. In order to interact with target nuclei in this manner, a positively charged particle must overcome the repulsive electromagnetic force exerted as it approaches the nucleus. The minimum energy to overcome the coulomb force is termed the coulomb barrier and is expressed in MeV by $U_{coul} = 1.03 \times \frac{1+A_1}{A_2} \times \frac{Z_1 Z_2}{A_1^{1/3}+A_2^{1/3}}$ where Z_1, A_1 refer to the incident ion's atomic number and atomic mass respectively and Z_2, A_2 refer to the target atom's atomic number and atomic mass respectively [41]. These interactions do not require the conservation of kinetic energy as they can leave a target nucleus in an excited state or even lead to spallation, resulting in high energy fragments.

The specifics of coulombic and non-coulombic nuclear interactions will not be discussed in detail as this work focuses primarily on high energy ions found in the space environment for which the primary energy loss mechanism is coulombic interactions with the electron cloud of a target. However, because nuclear reactions can significantly contribute to error rates [41] and have traditionally been the dominant cause of SEU from light ions, relevant sections will take nuclear reactions into consideration for context.

II.2 Secondary Electron Generation and Physics

Energy lost by an ion due to electronic stopping is transferred to the electrons in the target material. This either ionizes the parent atom or leaves the parent atom in an excited state. An excited atom will de-excite back to its ground state. This can occur through several processes including the emission of a photon or an auger electron. Electrons which are freed from their parent atoms are termed secondary electrons or delta rays ($\delta rays$). Ion electron interactions can be approximated as a binary collision where the energy transferred to an electron is $T_{e-} = \frac{4m_1 m_2}{(m_1+m_2)^2} E \cos\theta$ [42]. In this equation, E is the energy of the incident ion, m_1 m_2 are the masses of the particles involved in the collision, and θ is the angle of emission from the ion path. The maximum energy secondary electron produced by a incident ion then occurs at $\theta = 0$ and has energy $T_{max} = \frac{4m_1 m_2}{(m_1+m_2)^2} E$. From the binary collision

approximation, it also apparent that low energy electrons are ejected perpendicular to the direction of ion travel. Ion electron interactions are random in nature. The differential probability of transferring an amount of energy T to a secondary electron is given by the Rutherford cross section as $d\sigma = \pi(\frac{b}{2})^2 T_{max}(\frac{dT}{T^2})$ [43], where b is the impact parameter. From the Rutherford cross section, it is seen that the probability of producing a secondary electron decreases as the square of its energy. The spectrum of secondary electrons produced by an ion is then dominated by relatively low energy secondary electrons.

Once freed from their parent atom, secondary electrons move throughout a material, losing energy as they interact with it. Secondary electrons interact with matter through three mechanisms: elastic scattering, bremsstrahlung emission, and inelastic collisions. Elastic scattering occurs when an electron interacts with the nucleus of an atom. In this interaction, electrons scatter off a target nucleus without altering its quantum state. These interactions serve primarily to change the direction the secondary electron is travelling as the energy lost to the recoiling nucleus is negligible due to the large mass of the nucleus relative to an electron. Bremsstrahlung, or breaking radiation, is the emission of a photon by an accelerating charged particle. Electrons travelling in material emit bremsstrahlung due to acceleration caused by the electrostatic field of atoms. Finally, the primary energy loss mechanism for low and medium energy electrons is inelastic collisions. Inelastic collisions occur between the energetic electron and electrons contained in the medium through which they travel [40]. These collisions result in electronic excitation or ionization, creating more secondary electrons. The time evolution of the F of secondary electrons generated by a 5 keV primary electron travelling in Si is shown in figure II.2.

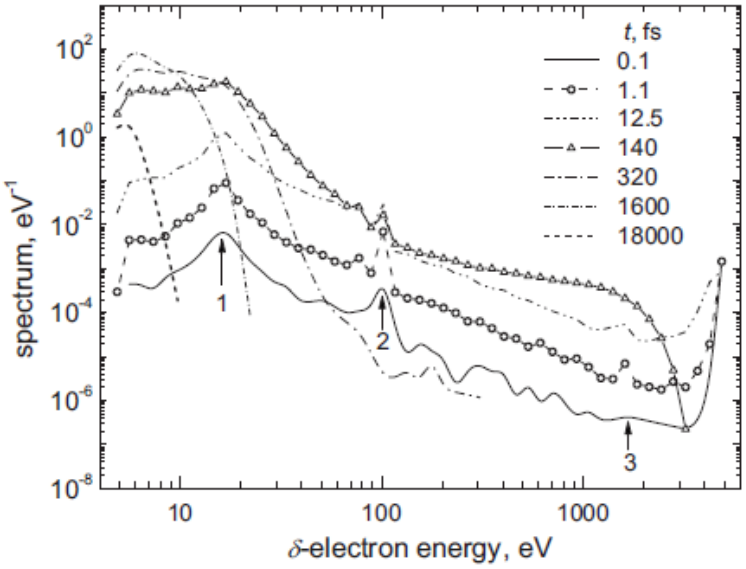

Figure II.2: Time evolution of the spectrum of generated secondary electrons per primary electron with energy 5 keV in silicon. As the primary electron loses energy over time, the spectrum of secondary electrons which it can produce shifts lower in energy. The arrow at 16.7 eV indicates a plasmon peak in silicon. Arrows at higher energies show shell edges of silicon [4].

Eventually, a secondary electron loses all of its excess energy and thermalizes back into the bands of the material through which it is travelling. Figure II.3 provides information on the amount of time this process takes by showing the total number of cascading electrons, including those that have already stopped, as a function of time for different primary electron energies. When the incident electron and the secondaries it produces are settled, no further secondary electrons are produced, and the number of cascading electron saturates. This occurs for primary electrons of all energies by around 1 ps. This is typically fast enough to be considered instantaneous from the point of view of microelectronic device response; however, plasma effects have been observed in charge collection measurements performed with high speed photodetectors [4].

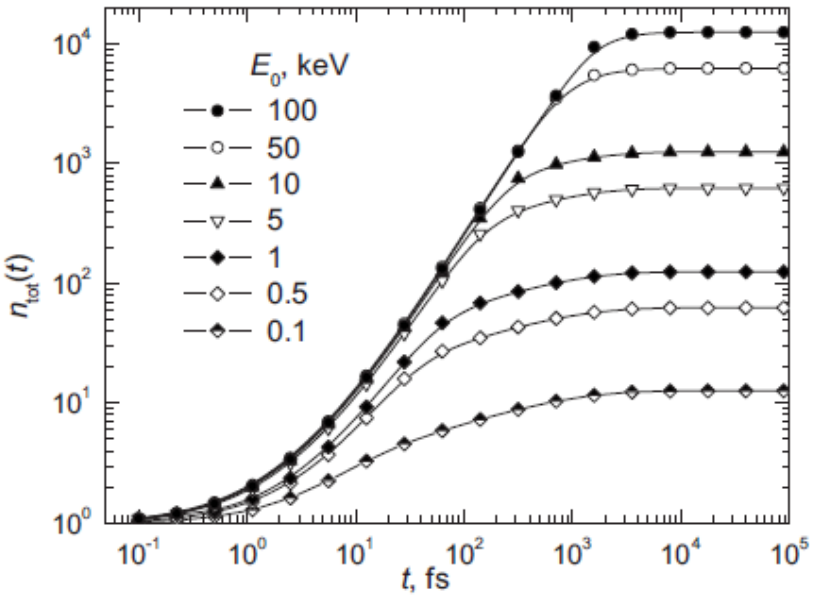

Figure II.3: Total number of cascading electrons, including those that have stopped, created by an incident electron of energy E_0 as a function of time [4].

The distance secondary electrons travel before they settle is of interest because it determines the volume over which an ion may cause charge to be generated as well as the density of the generated charge. The simplest approximation that can be made to determine the range of a secondary electron of a given energy is the continuous slowing down approximation (CSDA). The CSDA assumes that an electron travels in a linear path with the total distance travelled given by the integral of the electron's stopping power as $\int \frac{dE}{-\frac{dE}{dx}}$ [4].The CDSA overestimates the range of electrons, especially those of low energy, because elastic and inelastic scattering events randomize the path taken by an electron. The inverse mean free path to a scattering event for electrons is calculated by Akkerman using Monte Carlo methods and is shown in figure II.4. Akkerman goes on to calculate the range of electrons taking into account scattering events and provides a comparison to CSDA as shown in figure II.4. The CSDA overpredicts the range of electrons at all energies and is particularly bad for low energy electrons for which it overpredicts the electron range by over an order of magnitude.

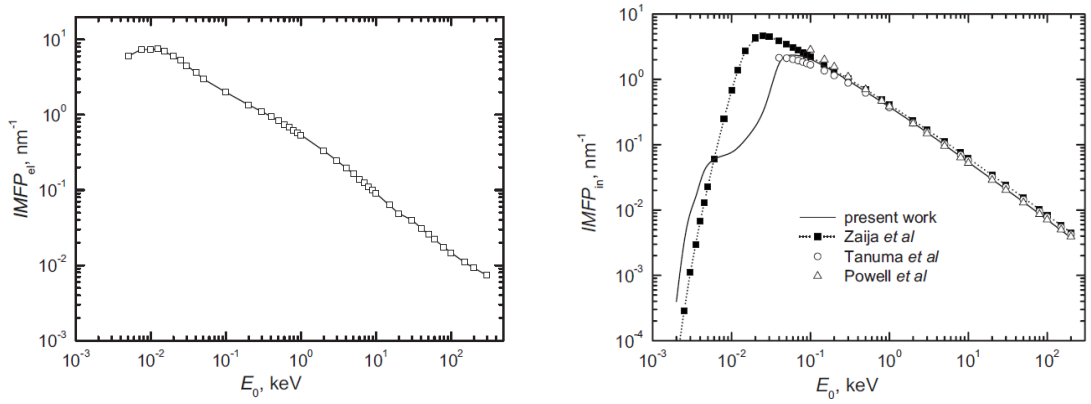

(a) Inverse mean free path to elastic scattering

(b) Inverse mean free path to inelastic collision

Figure II.4: Figures (a) and (b) show the inverse mean free path to an elastic and inelastic scattering event respectively for an electron of specified energy. Scattering events alter the direction of motion of an electron limiting their practical range [4].

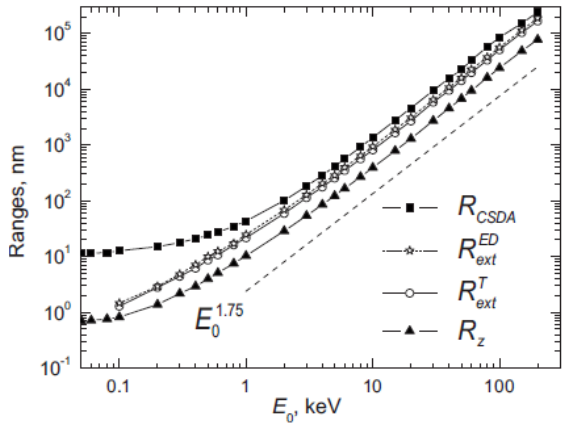

Figure II.5: Comparison of electron range for different stopping theories. R_{CSDA} denotes the continuous slowing down approximation and R_z denotes the result of Akkerman's Monte Carlo code which takes into account scattering events which limit the practical range of electrons, particularly at low energies [4].

Early studies of free electron range in materials relied on transmission of electrons through metallic foils to determine semi-empirical formulas which accurately describe the practical range of energetic electrons in matter. This work was applied by Kobetich and Katz to determine the ionization track structure of an ion. Ionization track structure describes the average energy (dose) deposited by secondary electrons at a radial distance

from the ion path. By placing concentric cylinders around the ion path, and calculating the average energy deposited by secondary electrons in each cylindrical shell, the ionization track structure of an ion can be determined. This calculation is further simplified by assuming all secondary electrons are ejected normal to the ion path. This assumption is valid over distances relevant to the ionization track structure, because the dose deposited over these distances is deposited primarily by low energy secondary electrons which, from the kinematic equation, must be ejected normal to the ion path. The resulting relation between dose and distance from the ion path is given by $\frac{E}{z_{eff}^2} \propto \frac{1}{t^2}$. That is the average dose of deposited energy, E, is directly proportional to the effective charge state of the ion, z_{eff}, and inversely proportional to the square of the distance from the ion track, t [44].

II.3 Energy Loss Spectrum

Energy loss by an ion travelling through a material is a random process. There will, therefore, be fluctuations in the amount of energy lost by individual ions passing through the same material even for a monoenergetic beam. The spectrum of energy loss is typically displayed either as a differential spectrum or an integral spectrum. In a differential spectrum, the y-axis is the differential number of events (dN) which lose an amount of energy while the x-axis is the amount of energy lost. The total number of events which lose an amount of energy between x_1 and x_2 is then simply $\int_{x_1}^{x_2} \frac{d\mathrm{N}}{dx} dx$. The integral spectrum is simply the back integral of the differential spectrum. That is to say it displays the total number of events (y-axis) which deposit an amount of energy x_1 or greater. The same information is present in both spectra, and one can be obtained from the other. Figure II.6 displays this relationship.

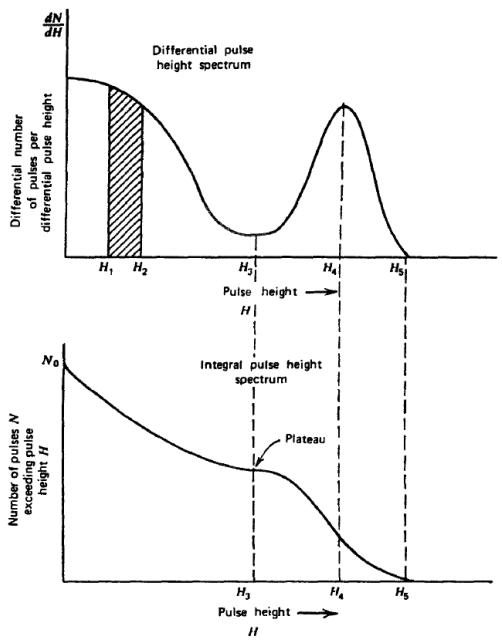

Figure II.6: Relationship between differential and integral spectra, applied in this figure to the recording of the distribution of pulse heights produced by a radiation source interacting with a detector. The spectra portray the same information and are calculable from one another [5].

The differential spectrum directly samples the underlying probability distribution describing energy loss by the ion. In practice, events are typically histogrammed. Each bin in a histogram is the integration of the underlying distribution over that bin. As the bin width (δt) of a histogram goes to zero, the number of counts in the bin (n_i) converge to be proportional to the value of the distribution (f) at the center of the bin. That is to say, for small bin widths, $n_i \propto N\delta t f(t_i + \frac{\delta t}{2})$. In practice, bin widths often increase logarithmically in size in order to cover a large range. Because this results in an unequal range of integration over different parts of the underlying distribution, the histogrammed data gives a skewed image of the underlying probability distribution. In order to view the true differential spectra, the histogrammed data should be scaled by the bin width. That is to say that $\frac{n_i}{\delta t_i} \propto N f(t_i + \frac{\delta t_i}{2})$ [45].

The first moment of the energy loss distribution has already been introduced as the ion's stopping power. The second moment of the energy loss distribution is termed the energy

loss straggling (denoted σ^2) with the square root of the second moment (the standard deviation) being termed the energy loss fluctuation. The ratio $\frac{\sigma}{\overline{\Delta E}}$, where $\overline{\Delta E}$ is the average energy loss in a film of thickness d_0, is a useful measure of energy loss fluctuation. Energy loss straggling for protons in silicon was calculated by Akkerman and extended to heavier ions with the expression $\frac{\sigma}{\overline{\Delta E}} = \frac{10^{\alpha}}{Z_{eff}\sqrt{d_0}}$ [10]. In this expression α is a fitting paramter given by $\alpha = -1.02428 + 0.68676 + 0.04904x^2$ with $x = \log_{10} E$ with E being the ion velocity in MeV u^{-1}. Z_{eff} is the effective charge of the ion which can be calculated using the expression $Z_{eff} = Z[1 - exp(-125\beta Z^{-2/3})]$ where $\beta = \frac{v}{c}$ is the ion velocity relative to the speed of light. For ions which are not fully stripped, fluctuations in the effective charge state of the ion can significantly increase energy loss straggling. In general, energy loss straggling increases with decreasing path length, decreasing atomic number Z of the incident ion, and increasing incident ion energy.

CHAPTER III

Limitations of LET as a Metric for Radiation Effects Analysis

III.1 Ionization Track Structure

The utility of LET as a metric for use in SEU rate calculations has been questioned since at least as early as 1988 by Stapor [6]. Stapor noted that particles with similar LETs can have very different track structures. Even particles of the same species but different energies can have a similar LET and very different ionization track structures due to the different spectrum of secondary electrons they produce. This is illustrated in figure III.1 which shows calculated ionization track structures for two sets of ions of the same species and LET but different energies: 391 MeV Ni, 20.4 MeV Ni, 47 MeV Cl, and 19.2 MeV Cl. The charge collected by a Silicon on Sapphire (SOS) CMOS device when exposed to these sets of ions is shown in figure III.2. The less energetic ion in each set resulted in less collected charge despite the similar LET, and, therefore, similar amount of charge generated as the high energy ion. This is due to the low energy ion producing a higher density of generated charge. This higher density of generated charge leads to more initial recombination of generated carriers, leaving less carriers to be collected.

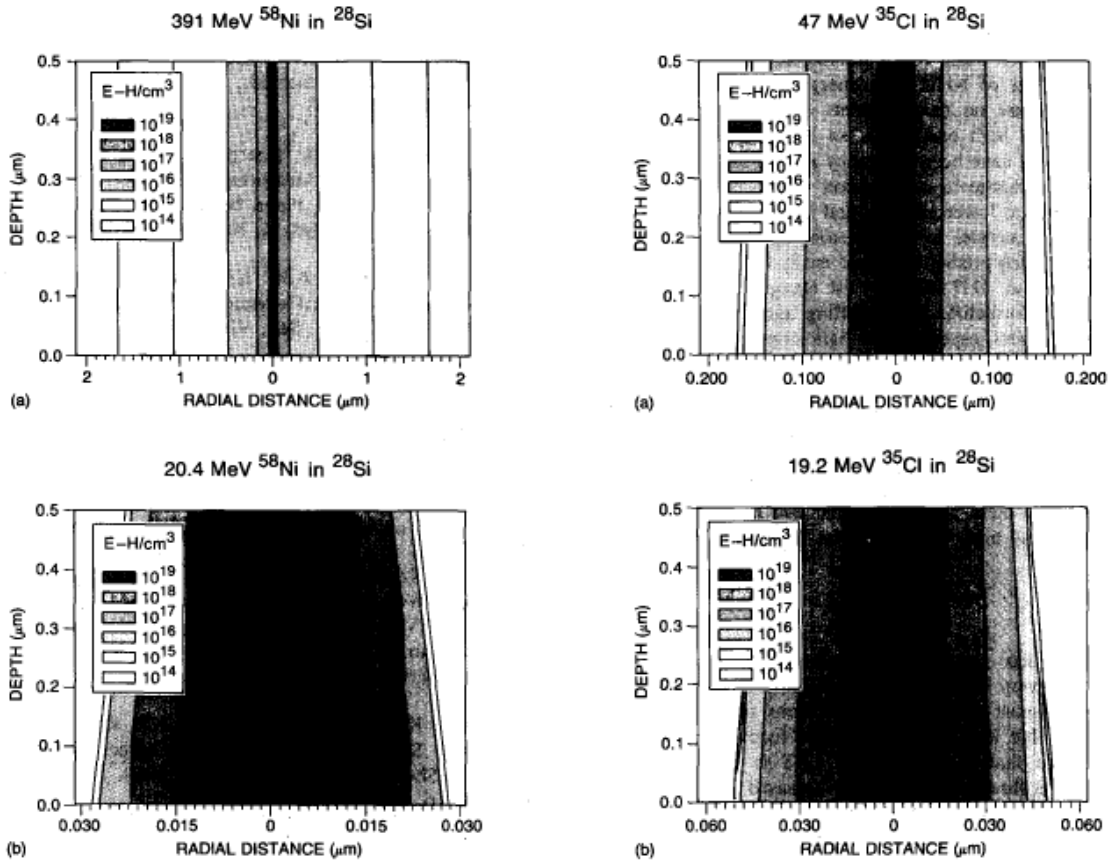

Figure III.1: Calculated ionization track structure for two sets of ions of the same species and LET but differing energies. In each set, the low energy ion's ionization track structure is more dense than the high energy ion's ionization track structure due to the higher maximum energy of secondary electrons produced by the high energy ions [6].

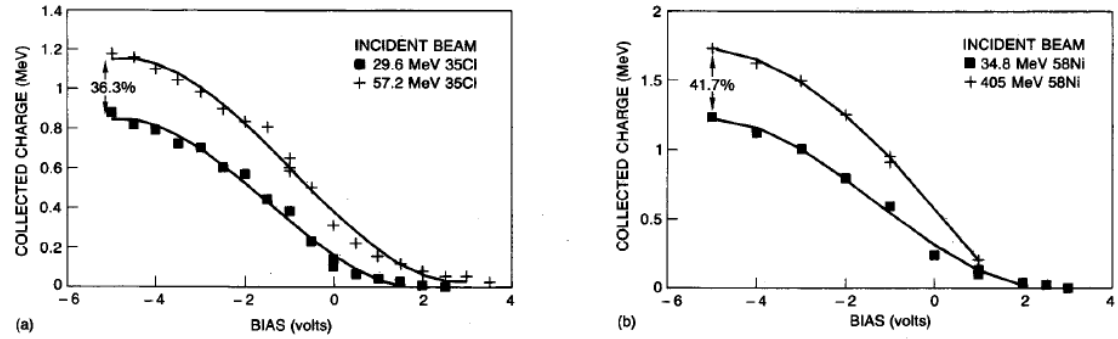

Figure III.2: Total collected drain current as a function of applied bias for a silicon on sapphire CMOS device exposed to two sets of ions of the same species and LET but differing energy. The collected charge is higher for the high energy ion of each set because the density of generated carriers is lower, leading to less initial recombination and allowing for more of the generated charge to be collected [6].

The effect of track structure on bit error rates is an important question due to the use of relatively low energy ion beams to predict upset rates by energetic heavy ions in space on an LET basis. As a result, Dodd investigated ion track structure effects in SRAM down to the 0.5 µm node and concluded that track structure effects did not impact the bit error rate [7]. This was theorized to be due to the similarity in charge density of the inner track radius of low energy and high energy ions as shown in figure III.3. However, the possibility of track structure effects impacting error rates in smaller technology nodes which would be sensitive to the low density of charge generated in the outer ion track was not ruled out. This could impact single bit error rates as near misses by energetic ions could deposit enough charge to cause an upset. It could also impact multiple bit error rates as the distance spanned by the outer ionization track of high energy ions is large enough to affect multiple junctions.

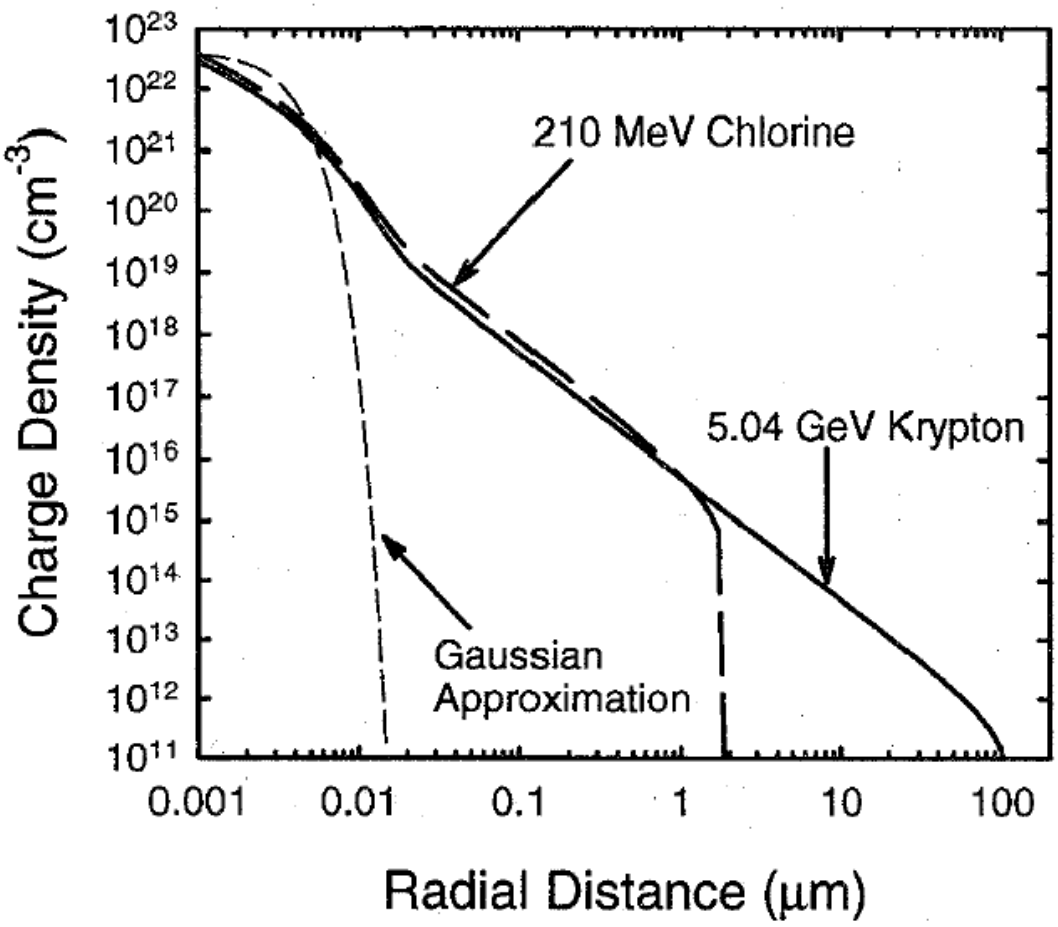

Figure III.3: Calculation of the generated charge density as a function of distance from the ion track for two ions with similar LETs but very different energies. The generated charge in the inner track, less than approximately 250 nm from the ion track is remarkably similar. Also shown is a Gaussian approximation of generated charge. Gaussian approximations are commonly used in device response simulations [7].

As technology has continued to scale, there has been further evidence that the microstructure of the ionization track is becoming relevant. In device response simulations, it is common to model an ion strike as cylinders of deposited charge corresponding to the conventional ionization track structure. This is inherently an average event and does not capture the actual ion track, made up of discrete secondary electrons, of any single event. Ejected electrons which travel near the channel can have a non-linear impact on the device response. Weller shows that an event which deposits only a few times the LET of energy results in a device response orders of magnitude larger than seen using the conventional

LET track structure due to the microstructure of the track [46]. Furthermore, the ability of secondary electrons to deposit large amounts of energy in very small regions of space due to an inelastic scattering event limits the utility of an averaged ion track structure in determining effects in highly scaled devices. As seen in figure III.4, the maximum energy deposited by secondary electrons in a 50 nm Si cube remains relatively constant out to radial distances far beyond where the Katz model would predict any energy deposition at all. Electrons have been shown to cause single event upsets in highly scaled devices [47]. This raises possibility that discrete secondary electrons produced by energetic ions could produce errors many microns away from the initial strike location, hampering hardening schemes which rely on physical separation of nodes, such as bit interleaving, and significantly contributing to the overall error rate.

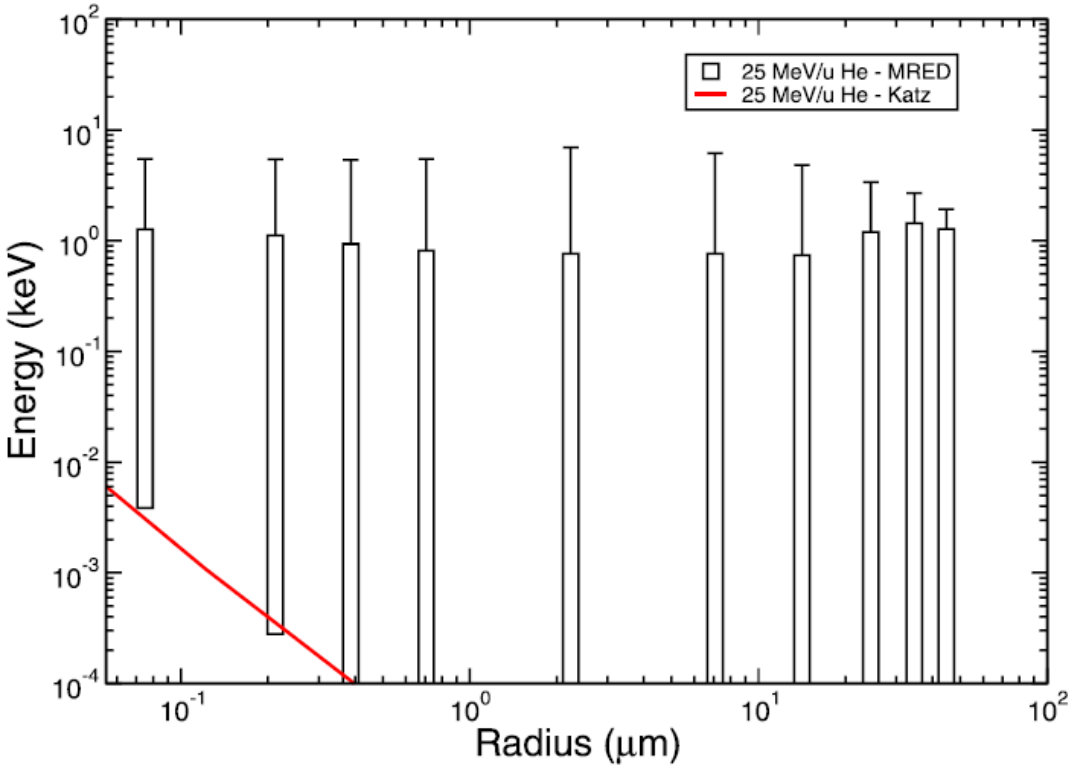

Figure III.4: Boxes show energy deposition in a 50 nm silicon cube at the specified radial distance from the track of a 25 MeV He ion. The bottom of the box shows the average energy deposited and is in good agreement with the Katz model for ionization track structure. The top of the box shows the 90th percentile of energy deposited in the box with the whisker showing the maximum energy deposition event [8].

III.2 Limitation of LET Metric in Small Volumes

An underlying assumption in the use of LET in conventional error rate calculations is that all of the energy lost by an ion is deposited in the sensitive volume. However, as has been shown in the previous section, the ionization track structure can be very large, and the most energetic secondary electrons produced by ions found in the space environment can travel more than a hundred microns in silicon. This essentially guarantees that charged particle equilibrium will not exist in a small volume as even if charge particle equilibrium exists along the ion track, secondary electrons will escape radially from the sensitive volume [9]. The fraction of energy lost by an ion which is deposited in a sensitive volume is shown in figure III.5. This has implications for SEU testing as the limited number of ion species and

energies available necessitate the use of angled testing to fill in the LET vs upsets curve. These tests rely on the ion to deposit more energy in the sensitive volume due to the longer path length the ion takes through the sensitive volume. The response is then assumed to be analogous to that of an ion whose LET is such that it deposits the same amount of energy in the sensitive volume at normal incidence. As devices scale, this type of testing may no longer provide accurate results, because the amount of charge an ion deposits in a sensitive volume will be highly dependent on its velocity.

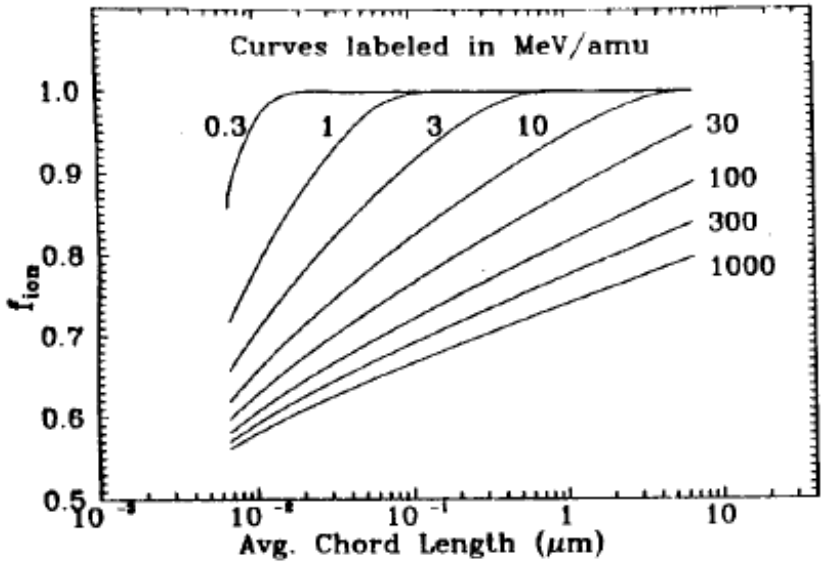

Figure III.5: The fraction of energy lost by an ion with specified kinetic energy which remains in a sensitive volume with a given average chord length (average distance a secondary electron must go to escape the volume). More energy escapes for smaller volumes (smaller average chord lengths) and higher incident kinetic energies [9].

A further limitation of LET in small volumes is the increase in energy loss straggling as volumes decrease in size. This is shown for helium in figure III.6. This limits the utility of the LET metric as it is an average of the energy loss distribution of an ion. The larger the variance of the distribution, the less well the average describes that distribution. For particles lighter than carbon, energy loss straggling in small volumes can be so significant that it is larger than the LET [10]. In these cases, the average becomes practically useless as a metric for describing energy loss by the ion. The effect that decreasing volume size has on

the differential energy loss spectrum of 20 MeV protons is shown in figure III.7. As can be seen, despite the average energy lost by the 20 MeV proton trending towards zero as layer thickness decreases, the maximum energy lost remains relatively constant. The increase in straggling in thin volumes can be explained by a decrease in the average number of interactions the ion has with the electron cloud as it passes through this volume. For light ions, the average number of interactions becomes so low that straggling overtakes LET. For heavy ions, the number of interactions remains sufficiently high for LET to remain useful in describing energy loss.

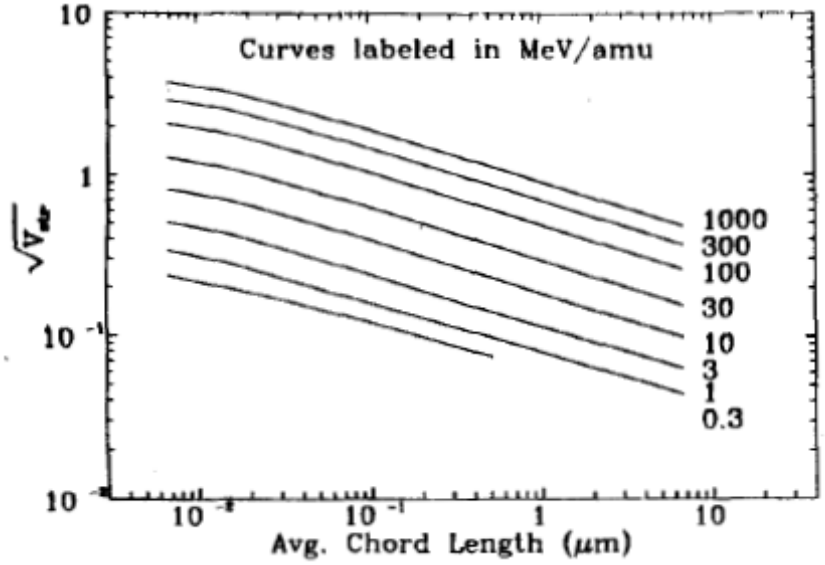

Figure III.6: Calculation of the fluctuation in energy deposition by isotropic helium of specified velocity in silicon sensitive volumes as a function of the average chord length travelled through that volume. Fluctuations in the deposited energy increase for increasing helium energy and decreasing average chord length of the volume [9].

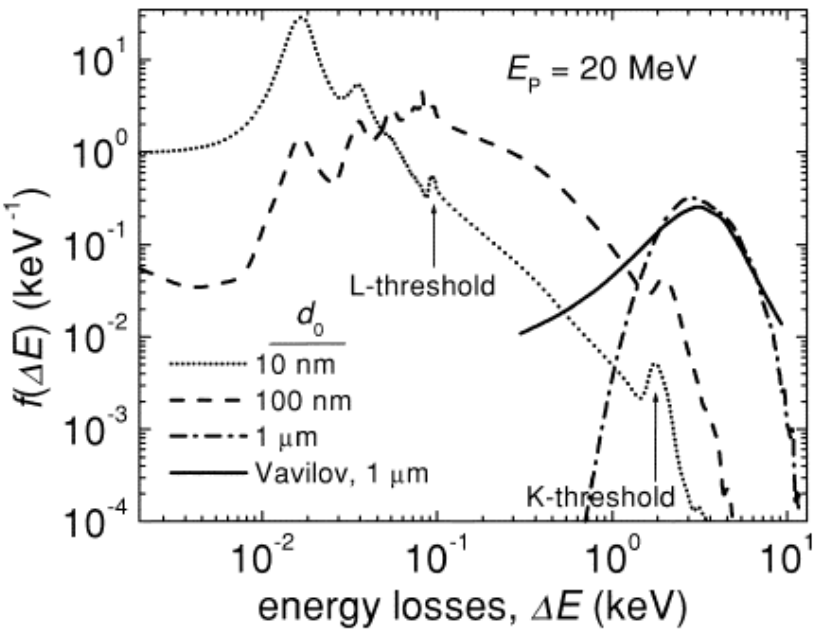

Figure III.7: Probability density function of the energy lost by 20 MeV protons in silicon of specified thickness. The energy peak at 16.7 eV is a plasmon excitation with higher energy peaks corresponding to shell edges as labled [10].

III.3 Dose Enhancement

Materials surrounding a sensitive volume can impact the amount of energy a radiation source deposits in the volume. The dispersion of secondary electrons at a material interface results in a situation in which charge particle equilibrium is not in place. This can result in the deposition of a larger amount of energy than would be predicted in an equilibrium case. The deviation in deposited energy from equilibrium is expressed with the dose enhancement factor (DEF) where $\text{DEF} = \frac{\text{average dose in sensitive region}}{\text{equilibrium dose}}$. This phenomenon has traditionally been studied primarily in regards to its effects on TID and thus has been termed dose enhancement. The source of radiation in these cases has been limited to x-ray and gamma-ray sources. Dose enhancement occurs within an electron range of a material interface. In this range, the difference in number and nature of secondaries produced by a radiation source in the two materials forces the system out of equilibrium such that the

dose deposited in either material differs from the equilibrium dose. Dose profiles at a gold silicon interface under x-ray and gamma-ray irradiation are shown in figure III.8.

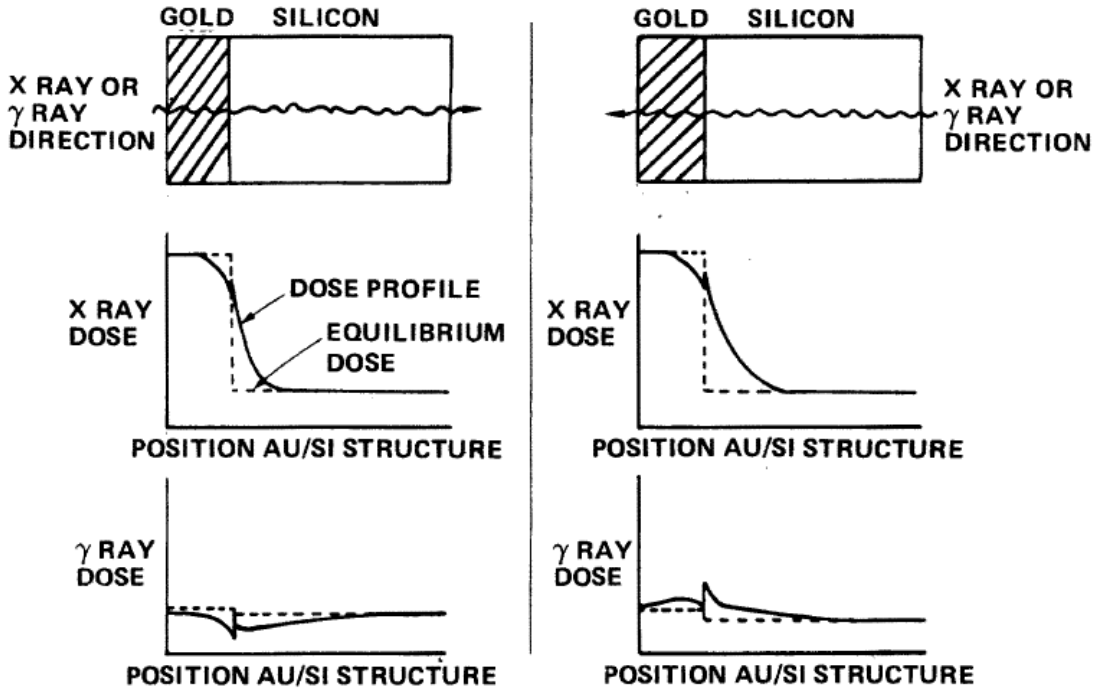

Figure III.8: Dose profiles at a gold-silicon interface under x-ray and gamma-ray irradiation in the direction specified by the arrow. The equilibrium dose profile is shown by the dotted line [11].

As seen in figure III.8, the deposited dose at a material interface is strongly dependent on the radiation source. Differences between the gamma-ray and x-ray dose profiles can be explained by the different ways the radiation interacts with matter. X-rays deposit energy in a material primarily through the photoelectric effect. Photon absorption in this process is strongly dependent on the atomic number Z of the material through which the photon is travelling. The absorption cross section for a photon in a high-Z and low-Z material can be several orders of magnitude different. The multitude of electrons generated in the high-Z material penetrate the low-Z material, enhancing the deposited dose in the low-Z material and reducing the deposited dose in the high-Z material. Furthermore, electrons generated by the photoelectric effect are ejected isotropically from their shell. This leads

to an independence of the dose distribution on the direction of the incident x-ray. Dose enhancement from x-rays peaks at a photon energy of around 100 keV with an enhancement factor of approximately thirty.

Gamma-rays typically have a photon energy higher than several hundred keV and lower than 10 MeV. In this energy range, photons lose energy primarily through Compton scattering. Compton scattering is largely independent of the material Z and produces secondary electrons which scatter in the direction the gamma ray is travelling. This leads to a dependence on the direction of the incident radiation on the dose profiles at material interfaces as seen in figure III.8. Because the cross section for Compton scattering is largely independent of the material Z, the dose profile at a high-Z low-Z material interface is largely determined by differences in scattering of the secondary electrons at the interface [11]. Gamma-rays incident on the low-Z side of a low-Z/high-Z interface lead to an enhancement of dose on both sides of the interface while gamma rays incident on the high-Z side low-Z/high-Z interface lead to a reduction in deposited dose on both sides of the interface [12]. The maximum dose enhancement factor due to gamma rays is around two.

CHAPTER IV

Energy Deposition due to Direct Ionization in Small Volumes

IV.1 Introduction

The radiation response of highly scaled microelectronic devices is explored using mred [39] and PENELOPE 2008 [40]. The underlying structure of mred is the GEANT4 radiation transport code [37]. In this work, GEANT4 codes are used to simulate the transport of a primary ion while the transport of secondary electrons produced by a primary ion is simulated with PENELOPE 2008. As a indicator of the degree to which PENELOPE 2008 is significant to this work, mred calculations which utilize the PENELOPE 2008 framework to calculate secondary electron transport will be denoted as mred+penelope.

Scaling in the microelectronics industry has pushed sensitive volume sizes to the nanometer scale. The energy loss distributions of light ions in small sensitive volumes is heavily influenced by the atomic structure of the material making up the volume. This is due to the low number of interactions a light ion has with the electron cloud as it passes through the sensitive volume. It is, therefore, necesssary to evaluate the utility of GEANT4 in determining energy deposition due to light ions in small sensitive volumes. This is primarily due to the ”continuous energy loss” abstraction used in GEANT4 radiation transport calculations. The continuous energy loss abstraction is a way of simulating energy lost by a particle which does not create a trackable secondary electron. In thin absorbers, GEANT4 relies on a simplified two energy level model of the atomic structure to simulate continuous energy loss. The exact energy chosen for these levels is determined in part by the mean ionization energy of the material [48]. This abstraction provides a useful and accurate means of describing energy loss by a particle over a relatively high number of interactions due to the inherent averaging which occurs over these interactions.

To determine the accuracy of mred+penelope in calculating energy deposition from light ions in small sensitive volumes, the energy deposition distributions of protons were compared to energy loss distributions of protons calculated by Akkerman et al. [10]. Akkerman performed these calculations with a Monte Carlo code based on the energy-loss function (ELF) $\mathrm{Im}(-1/\varepsilon(\omega,q))$. In this function $\varepsilon(\omega,q)$ is the complex dielectric function where $\hbar\omega$ is the energy loss and $\hbar q$ is the momentum transfer. This method does not rely on the mean ionization energy of the material, and Akkerman provides several comparisons to confirm the accuracy of his code. A mockup of the mred target structure used in these simulations is shown in figure IV.1. The structure consists of a silicon sensitive volume with 5 µm of silicon on either side of the sensitive volume. This layer establishes some amount of charge particle equilibrium and is roughly representative of material surrounding a microelectronic device. The Energy deposition due to 20 MeV protons in the sensitive volume is calculated for sensitive volumes of thicknesses 1 µm, 100 nm, and 10 nm.

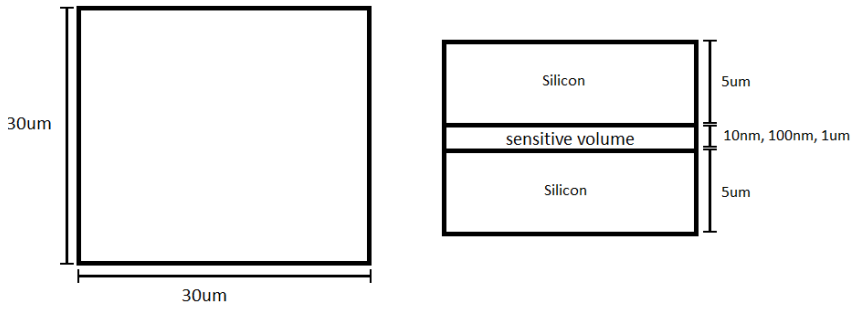

Figure IV.1: Mock up for the target structure used in comparing energy deposition due to direct ionization by protons as calculated by mred+penelope to energy loss calculations for protons performed by Akkerman in [10]. All layers are silicon. The Layers on either side of the sensitive volume are 5 µm thick and provide some amount of charge particle equilibrium. Energy deposition was calculated for sensitive volume thicknesses of 1 µm, 100 nm, and 10 nm.

The energy loss distribution for 20 MeV protons in silicon as calculated by Akkerman is compared to the energy deposition distribution for 20 MeV protons in silicon as cal-

culated by mred+penelope in figure IV.2. In order to make the comparison, a minimum mean square error (mmse) normalization was applied to the distributions obtained from mred+penelope. The mred+penelope histograms are originally given in counts which specify the number of particles which deposited a given energy in the sensitive volume. The histograms are then scaled by bind width, because the histogram bins are logarithmically spaced. This provides an accurate representation of the underlying probability density function. The mred+penelope distribution and the Akkerman distributions are then compared, and it is assumed that they are the same except for a constant scaling factor. This assumption is made, because the accuracy of Akkerman's results and the accuracy of GEANT4 in relatively large volumes have been extensively investigated, and the energy loss and energy deposition distributions should be exactly the same in large volumes. The scaling factor which minimizes the mean square error between the mred+penelope and Akkerman distributions is selected as the normalization for the mred+penelope data. This is necessary because the scaling used in Akkerman's data is unknown. While this method limits our ability to discern a difference in the magnitude of the two distributions, it does not affect the relative probability of an event within a distribution.

In our opinion, the differences in results in the 1 µm sensitive volume is due entirely to the fact that Akkerman is calculating energy loss by a proton over 1 µm transport in silicon while mred+penelope is calculating energy deposition in a 1 µm sensitive volume due to the proton. Because energy lost by the proton creates secondary electrons which can travel microns in silicon, energy deposition in the sensitive volume is influenced by energy loss in surrounding materials. Even if charge particle equilibrium exists in the aggregate, it is not required to exist in a singular event. The energy deposition distribution at any point in the sensitive volume is then a convolution of the energy loss distributions within a secondary electron range of that point.

In the 10 nm sensitive volume, differences in the proton energy loss distribution and the proton energy deposition distribution occur for a number of reasons. The accuracy of

the energy deposition distribution below several hundred eV is limited by the continuous energy loss abstraction in GEANT4. This leads to many of the minute structure, including the plasmon peak at 16.7 eV, to be washed out. It is believed, however, that the energy deposition distribution is accurate for events which deposit more than several hundred eV in the sensitive volume. The disappearance of the k-shell peak in the energy deposition distribution is attributed to secondary electron movement out of the sensitive volume. Energy loss events of this magnitude are likely to lead to an auger electron with enough energy to travel significant distances in silicon.

Somewhat counterintuitively, the energy deposition distribution calculated by mred+penelope is more accurate for higher energy protons. This is because a larger proportion of the energy loss by high energy protons results in a secondary electron with energy sufficiently high to be explicitly simulated. These electrons are simulated with PENELOPE 2008 which accurately simulates electron transport down to an electron energy of 50 eV. Figure IV.3 shows the energy deposition distribution of 100 MeV protons in a 10 nm thick silicon sensitive volume. The plasmon peak at 16.7 eV is clearly present as is the excitation peak corresponding to the L-shell of silicon at approximately 100 eV.

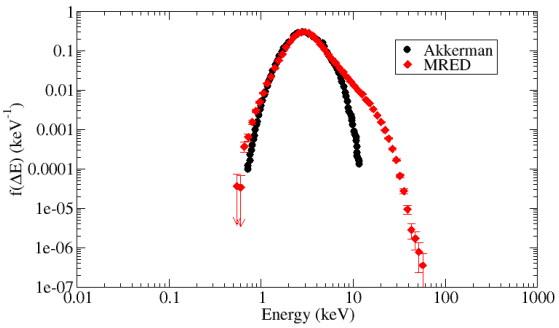

(a) 1 µm sensitive volume depth

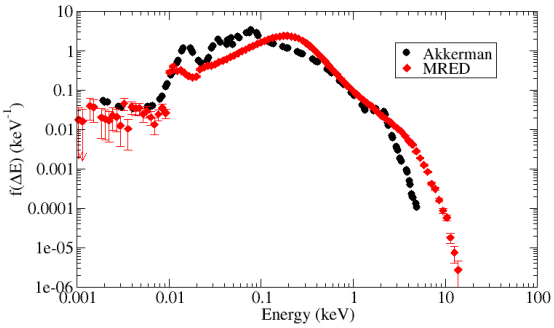

(b) 100 nm sensitive volume depth

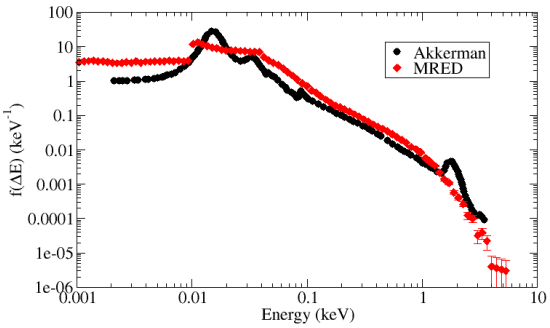

(c) 10 nm sensitive volume depth

Figure IV.2: Comparison of energy deposition distributions for 20 MeV protons calculated by mred+penelope with energy loss distributions for 20 MeV protons calculated by Akkerman in [10]. The mred target structure used in these calculations is shown in figure IV.1.

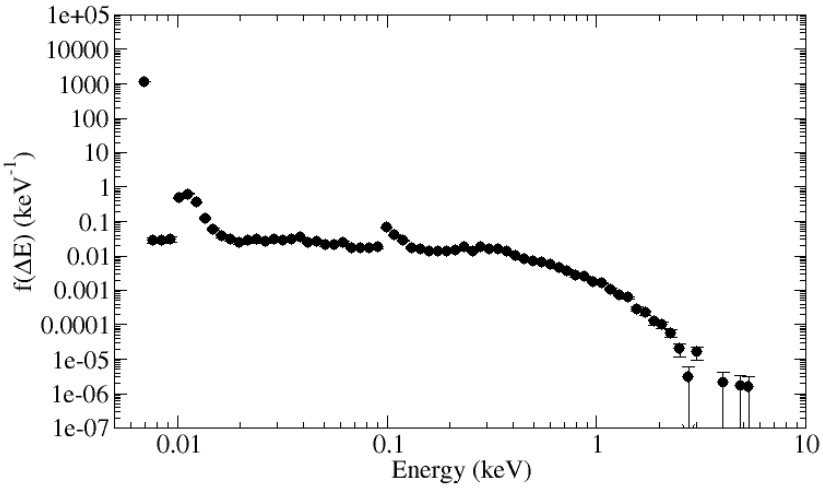

Figure IV.3: Energy deposition distribution for 100 MeV protons in a 10 nm thick sensitive volume. The peak at 16.7 eV is a plasmon peak. The peak near 100 eV corresponds to the L-shell threshold of silicon. The low energy point occurs due to the continuous energy loss abstraction in GEANT4 and is the minimum amount of energy the proton can lose as it passes through the sensitive volume. The mred target structure for this calculation is shown in figure IV.1.

IV.2 Impact of High-Z Material on Direct Ionization Energy Deposition by Ions

Poly depletion and quantum tunneling have necessitated the use of metal gates and high-κ dielectrics to continue device scaling [16, 17] while the need to reduce series resistance has led to metal silicide and metal clad source and drain regions [24]. Additionally, high-Z materials have made their way into the back-end-of-line of advanced processes in the form of tungsten vias. The effect these material changes have had on the deposited dose due to x-rays has been studied [49, 50], and the wider phenomenon of dose enhancement in x-ray and gamma-ray radiation environments is well known [11, 12]. The effects these materials changes have had on the system level nuclear reaction cross section, and as a result the SEU cross section, is also well documented [51]. However, the impact the use of high-Z materials near sensitive volumes has on energy deposited in that volume due to direct ionization from an ion, to the best of our knowledge, has not been explored.

To explore the impact of high-Z materials on energy deposition in sensitive volumes due to direct ionization by ions, mred+penelope simulations utilizing the target structure in figure IV.4 were preformed. The target structure is based on the target structure used in [52]. It is representative of a 3 metallization FDSOI process. The back-end-of-line consists of alternating layers of Al and SiO_2 as well as two W vias. The sensitive volume is a 5 nm thick layer of silicon which is consistent with the body depth of advanced SOI technologies [26, 27]. Below the sensitive volume is a 400 nm thick buried oxide (BOX), and below the BOX is 6.6 µm of silicon representing the wafer. Directly above the silicon sensitive volume is a tungsten contact layer 19.23 nm thick. Tungsten is the most electron dense material which has been proposed for use in gate stacks and source drain metallization. As such, the use of tungsten, and the placement of the contact directly above the sensitive volume body, represents a worst case scenario. As a control, the tungsten contact is replaced with silicon.

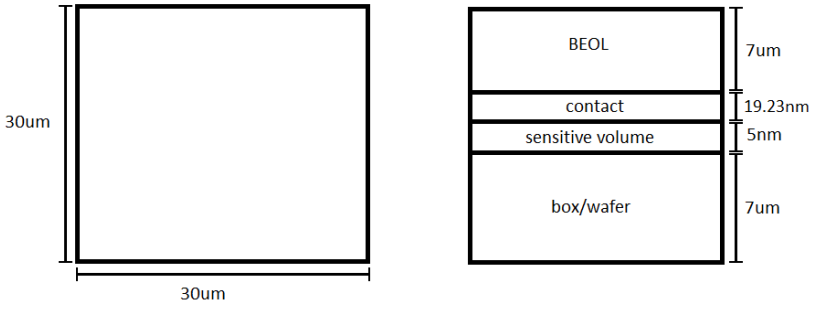

Figure IV.4: Mred target structure used for evaluating the impact of high-Z material on energy deposition in nearby sensitive volumes due to direct ionization by ions. The sensitive volume is 5 nm thick and made of silicon. The BEOL consists of aluminum and SiO_2 as well as two tungsten layers representing vias. The contact is a 19.23 nm layer of tungsten. As a control, the contact layer is switched to silicon.

The ion species H, He, C, O, Si, and Fe at energies ranging from 2.5 MeV u^{-1} to 10 GeV u^{-1} were simulated. These ion energies and species are representative of the make up of the majority of the galactic cosmic ray environment [2]. H ions up to ap-

proximately 400 MeV are also an abundant ion at orbits within the first Van Allen belt and contribute significantly to the total ionizing dose (TID) in this orbit [53]. Energy deposition in the silicon sensitive volume due to direct ionization from these ions was simulated using mred+penelope. An enhancement factor is calculated to quantify the effect the tungsten contact has on energy deposition in the sensitive volume. The enhancement factor is calculated as $\mathrm{EF} = \frac{\text{average deposited energy with tungsten contact}}{\text{average deposited energy with silicon contact}}$.

Figure IV.5a shows the calculated enhancement factor for the simulated ion species as a function of ion velocity for ions normally incident on the BEOL, referred to as the frontside. Figure IV.5b shows the calculated enhancement factor for ions normally incident on the wafer, referred to as the backside. The largest enhancement factor calculated is 1.2 and occurs for 2.5 MeV u^{-1} Fe incident on the frontside of the target. An enhancement factor of this magnitude is consistent with radiation energy loss processes which are largely independent of the material Z through which the radiation is travelling [11]. The trend of decreasing enhancement factor with increasing ion velocity is consistent with the change in the generated secondary electron spectrum as ions increase in velocity. As ion velocity increases, the spectrum of generated secondary electrons shifts higher in energy. The secondary electron environment in the sensitive volume at any specific energy is impacted by all secondary electrons generated with enough energy to reach the sensitive volume with that specific energy. As the spectrum of generated secondary electrons shifts higher in energy, the volume of the target structure which impacts the secondary electron environment in the sensitive volume increases. This reduces the enhancement factor as the secondary electron environment in the sensitive volume becomes more dominated by electrons generated in the BEOL and BOX/Wafer rather than those generated in the contact material.

For similar reasons, the observed enhancement in deposited energy is thought to be due primarily to low energy secondary electrons. This is also consistent with the lack of directional dependence of the enhancement factors observed for high energy silicon ions as seen in figure IV.5b. The direction a secondary electron is ejected from an ion track is

dependent on its energy. Low energy electrons are ejected normal to the ion track and have a low mean free path to a scattering event. This scattering event effectively randomizes their direction of motion, precluding a beam direction dependence on their energy deposition. As the silicon ion loses energy, the foreword scattering of secondary electrons becomes more pronounced. This leads to a higher enhancement factor for frontside irradiation, because frontside irradiation leads to the secondary electrons produced in the tungsten contact to be preferentially scattered forward into the sensitive volume while backside irradiation leads to secondary electrons produced in the tungsten contact to be preferentially forward scattered away from the sensitive volume.

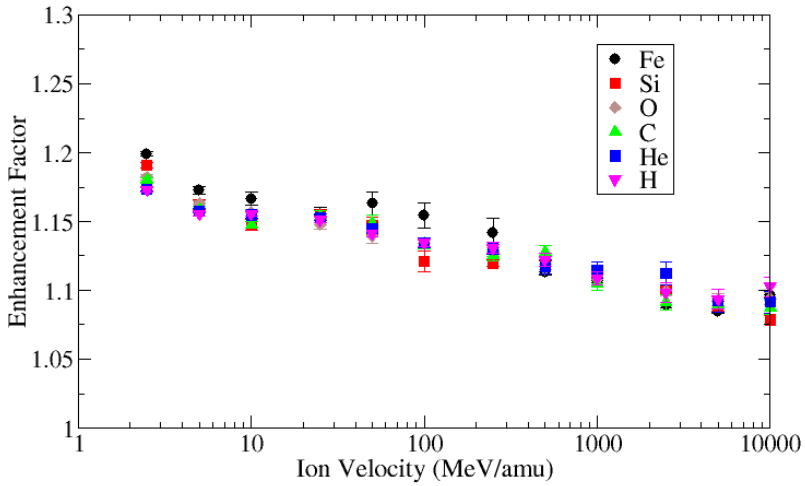

(a) Particle dependence of enhancement of energy deposition

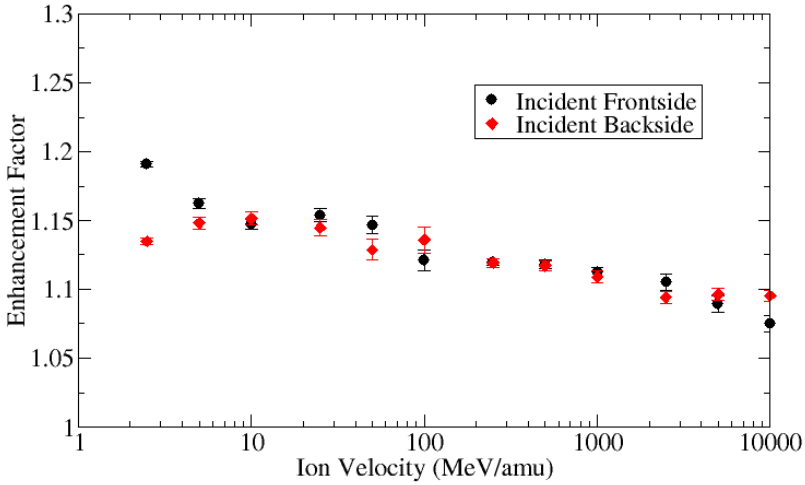

(b) Directional dependence on energy deposition due to a Si ion

Figure IV.5: Enhancement in the average deposited energy in the sensitive volume due to direct ionization by the specified ion. The mred target structure used in these calculations is shown in figure IV.4. Frontside denotes irradiation incident normal on the BEOL side of the target structure. Backside denotes irradiation incident normal on the wafer side of the target structure.

A worst case enhancement of the average deposited energy of an ion below a factor of two is unlikely to significantly impact either the total ionizing dose effects of protons or the SEU effects of heavy ions. However, it is worth exploring the impact that high-Z metallization may have on the SEU cross section for ions near the threshold LET. Near the threshold LET, the SEU cross section is extremely non-linear; therefore, even a slight increase in the energy deposition distribution of these ions may result in large changes in the SEU cross section. To study this, the energy deposition distribution of 2.5 MeV and 50 MeV protons incident normal to the frontside of the FDSOI structure as shown in figure IV.4 were calculated. Once again, a silicon contact was used as a control while a tungsten contact was used a worse case representation of gate and source/drain metallization. These energy deposition distributions were reverse integrated to give a cumulative probability of depositing a given energy or greater in the sensitive volume. The results are shown in figure IV.6.

For the high energy proton, the cumulative probability distributions for the tungsten contact and the silicon contact are virtually indistinguishable. For the low energy proton, the high-Z tungsten contact is seen to have a significant impact on the very highest energy deposition events, increasing their probability by nearly an order of magnitude. However, the cumulative probability distribution for the tungsten contact and silicon contact quickly converge, limiting the potential impact on the SEU cross section to a very narrow range of critical charge. Unfortunately, this range of generated charge is around the critical charge typical of unhardened circuits flown in space. While this result may warrant further investigation, mitigating factors, such as separation of the sensitive volume from high-Z material by gate oxides or a less dense gate material, may limit this effect in a real circuit. Overall, the use of high-Z materials near sensitive circuit elements is unlikely affect the system response to direct ionization by ions. However, this does not mean that high-Z materials do not impact the overall SEU rate of a system as high-Z material's impact on the nuclear

reaction cross section of a system is well documented and has been shown to significantly impact the SEU rate [36].

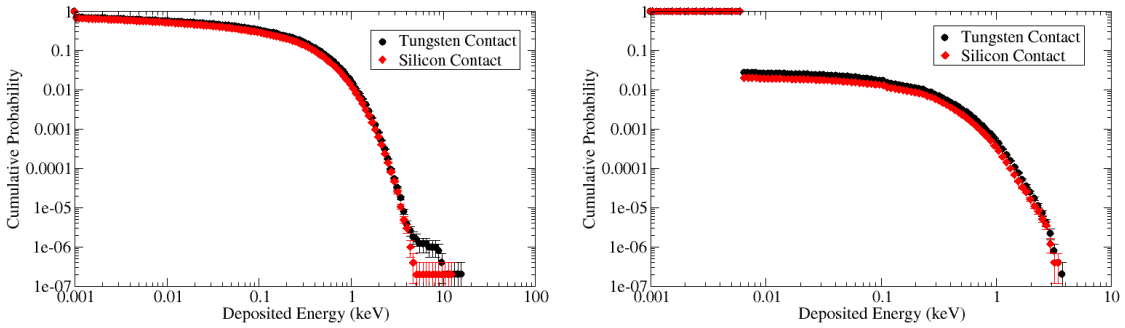

(a) Energy deposition from 2.5 MeV protons

(b) Energy deposition from 50 MeV protons

Figure IV.6: Probability of the incident ion depositing the specified amount of energy or more in the sensitive volume. The mred target structure used in these calculations is shown in figure IV.4.

IV.3 Effect of Energy Loss Straggling in Small Volumes

As the path length taken by an ion through a sensitive volume decreases, the energy loss straggling increases. For light ions, energy loss straggling can become larger than the average energy lost, limiting the utility of the LET metric [10]. SEU due to direct ionization from protons has already been reported in 65 nm technology [54]. Reducing critical charges as devices scale is likely to exacerbate the problem, and reduced sensitive volume sizes are likely to increase the importance of energy loss straggling in SEU error rate calculations. To investigate the realistic impact energy loss straggling has on error rates in highly scaled devices, the device target in figure IV.7 was used in mred+penelope simulations. The target structure is based on the target structures used in [55] and is representative of a 22 nm SOI SRAM cell. The sensitive volume is a silicon cube 50 nm to a side. The BEOL consists of alternating layers of aluminum and SiO_2 and is representative of a three metallization layer process. The BEOL also contains two tungsten layers representative of vias. Below

the sensitive volume is a 400 nm thick buried oxide (BOX), and below the BOX is 10 µm of silicon representing the wafer.

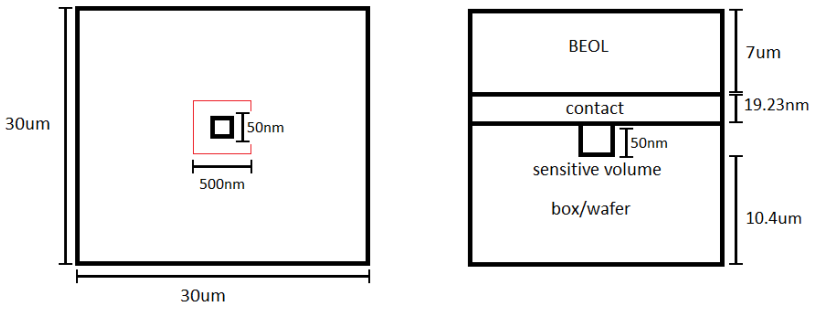

Figure IV.7: Mock up of the target structure used for mred+penelope simulations in determining the impact of energy loss straggling on SEU rates in advanced devices. The sensitive volume is a silicon cube 50 nm on a side and is representative of the sensitive volume of a 22 nm SOI SRAM cell. The BEOL consists of aluminum and SiO_2 with two tungsten layers representing vias. A directional flux was used to irradiate the sensitive volume. This flux was contained to the red box which is a square 500 nm to a side and centered on the sensitive volume.

The critical charge for this 22 nm SRAM cell was estimated in [55] to be 0.08 fC which is equivalent to 1.8 keV of energy deposited in the sensitive volume. A directional flux over a square 500 nm to a side and centered on the sensitive volume was irradiated with 10 MeV and 100 MeV H ions. The LET of these ions is 3.5×10^{-2} MeV cm^2 mg^{-1} and 5.9×10^{-3} MeV cm^2 mg^{-1} respectively. This gives a calculated average energy deposition for protons striking the sensitive volume at normal incidence of $\frac{dE}{dx}\Delta x = 405$ eV and $\frac{dE}{dx}\Delta x =$ 70 eV for 10 MeV and 100 MeV protons respectively. In an isotropic environment, the worst case chord length is $(x^2+y^2+z^2)^{1/2} = 86.6$ nm giving a worst case $\frac{dE}{dx}\Delta x$ of approximately 700 eV and 120 eV for the 10 MeV and 100 MeV protons respectively. Even the worst case $\frac{dE}{dx}\Delta x$ for these ions is several times lower than the estimated critical energy deposition, and, therefore, from a conventional SEU rate calculation perspective, direct ionization from these ions would not be expected to contribute at all to the SEU cross section of the SRAM.

Figure IV.8 shows the integral cross section for the energy deposition of 10 MeV and 100 MeV protons simulated in the 22 nm SOI SRAM device structure. The integral cross section is calculated by reverse integrating the energy deposition distribution and dividing by the fluence of simulated ions. All relevant physics was included in the simulation including nuclear interactions. The maximum energy deposited by direct ionization can be seen to be approximately 10 keV and 3 keV for the 10 MeV and 100 MeV protons respectively. Events which deposit more energy require a nuclear interaction of some sort. This is not necessarily spallation and could be a nuclear recoil or the backscatter of the incident proton back through the sensitive volume. The highest energy deposition events are likely due to a spallation reaction. Using the previously stated maximum energy deposition due to direct ionization, the nuclear reaction cross section, the cross section of an energy deposition event which occurs due to a nuclear interaction of some sort, is approximately 6×10^{-21} cm^2/bit for both the 10 MeV and 100 MeV protons. The SEU cross section, the cross section of depositing at least 1.8 keV, is 1.3×10^{-16} cm^2/bit and 1.7×10^{-18} cm^2/bit for the 10 MeV and 100 MeV protons respectively. Given these numbers, it is apparent that direct ionization, even by high energy protons, may play a significant role in determining the SEU cross section of highly scaled devices.

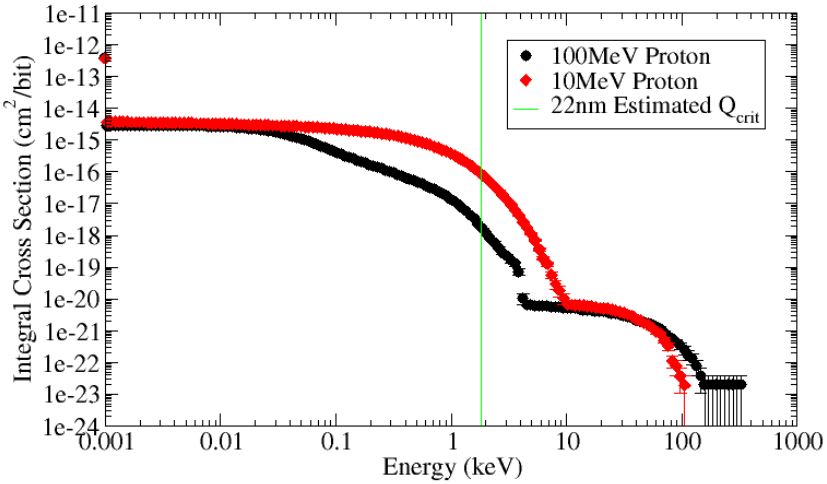

Figure IV.8: Integral cross section for energy deposition due to protons in a 22 nm SOI SRAM cell. The estimated critical charge for this technology 0.08 fC which is equivalent to an energy deposition of 1.8 keV. The mred target structure used in these calculations is shown in figure IV.7.

CHAPTER V

Conclusions

V.1 Conclusions of the Current Work

Monte Carlo simulations have been used to explore the impact scaling trends have on the radiation response of microelectronic devices. These simulations have been primarily focused on determining the impact that the incorporation of new materials into the microelectronic device structure and ever shrinking sensitive volume sizes has on energy deposition due to direct ionization by ions. This is critical to determining when and if the LET metric is useful for characterizing the radiation response of advanced devices.

The utility of mred+penelope in simulating energy deposition due to direct ionization from light ions in nano-scale sensitive volumes was explored. Energy deposition distributions for 20 MeV protons in silicon sensitive volumes of reducing thickness were compared to energy loss distributions of 20 MeV protons in the same thickness silicon volume as calculated by Akkerman. It was found that mred+penelope provided an accurate description of energy deposition events which deposited more then several hundred eV even in volumes as thin as 10 nm. Inaccuracy in the energy deposition distributions for events which deposit less than several hundred eV are thought to be due to the continuous energy loss abstraction used by GEANT4 in the calculation of energy loss by ions in thin absorbers. The actual inaccuracy in these distributions is thus difficult to determine as much of the energy deposition is done by discrete secondary electrons produced by the primary ion. These secondary electrons are simulated using PENELOPE 2008 which does not contain the continuous energy loss abstraction and is thought to model the energy loss by electrons to a high degree of accuracy even in thin absorbers.

The impact of the use of high-Z metals in gate stacks and as source/drain cladding on energy deposition in sensitive device regions due to direct ionization by ions was explored.

While some enhancement of the average amount of energy deposited due to direct ionization by ions was observed, the enhancement was always much less than a factor of two. Furthermore, the metal was not seen to significantly increase the number of high energy events. It is, therefore, unlikely that the incorporation of high-Z materials into gate stacks and source/drain cladding will have a significant impact on the microelectronic radiation response to direct ionization by ions.

The impact of energy loss straggling in the context of small volumes was explored. For light ions, energy loss straggling can exceed the average energy loss by several orders of magnitude in small volumes. Energy deposition by 10 MeV and 100 MeV protons in a target structure representative of a 22 nm SOI SRAM cell was simulated. From an LET viewpoint, direct ionization from these two particles should not impact the SEU cross section at all. However, the simulation results showed that, due to straggling, direct ionization from the protons significantly impacted the SEU cross section of the cell. This result is particularly important for evaluating error rates in orbits within the first Van Allen belt. Protons with energies up to 400 MeV are found in abundance in this region. As a result, SEU rate prediction methods for parts flown in this region may need to be revaluated to properly account for straggling effects which are not captured in the current LET metric.

V.2 Suggestions for Future Work

Many of the conclusions of this work rely on the accuracy of the mred+penelope fluctuation models. The accuracy of these models in thin volumes has not been rigorously explored. Energy loss spectrometry simulations should be performed with mred+penelope. These simulation results can be compared to Akkerman's caculations of relative energy loss straggling for protons in [10].

While agreement in results produced by mred+penelope with those produced by Akkerman is a positive sign, experimental evidence is needed to verify the results. To this end, SEU rate predictions made by mred+penelope should be compared to recorded proton error

rates in advanced devices. A good candidate for this kind of predictive SEU test would be the 14 nm SRAM which will soon be available. If possible, a specialized circuit should be designed to allow measurement of collected charge in an ultra-thin SOI device. The distribution of collected charge produced under high energy proton irradiation can be compared to energy deposition distributions calculated by mred+penelope, with a matching distribution verifying the results produced by mred+penelope.

Appendix A

Concepts and Limitations of mred

A.1 Range Cuts

GEANT4 offers great flexibility in simulation capabilities. One of the key components in maintaining this flexibility is the concept of range cuts. Range cuts in GEANT4 control the production electrons, positrons, and photons, which will be henceforth referred to as secondary particles or secondaries. Roughly speaking, for a secondary particle to be produced and discretely tracked, it must have enough energy to travel the distance in the material specified by the range cut. For instance if a range cut of 1 μm is set, all produced secondaries must have energy such that they can travel 1 μm in whatever material they are produced. However, once produced a secondary is tracked down to zero energy. The range cut value itself is not actually physically used anywhere in the simulations. That is to say that the set range cut value is translated into an energy value for each type of secondary particle in each material used in the simulation. These energy values are used in the simulation to determine whether or not an energy loss event produces a discrete secondary. All energy loss by particles below that required to produce a discrete secondary is approximated using continuous energy loss approximations.

The simplest continuous energy loss approximation is the use of an average rate of energy loss to all processes not discretely modeled by the production of secondaries. This approximation is used to simulate continuous energy loss by GEANT4 electrons. However, fluctuations in the continuous energy loss is also approximated for ions. In thick absorbers, continuous energy loss fluctuations are approximated by a Gaussian distribution with mean at the average loss. In thin absorbers, the approximation is more complicated and involves a simplified approximation of the atomic shell structure [48]. Range cuts are useful in allowing the size of simulated structures to vary widely. Small range cuts in large target

structures unnecessarily calculate energy deposition by short range secondary particles, wasting computational time. However, large range cuts skew energy deposition in small sensitive volumes.

The effect of large range cuts in small sensitive volumes is shown in figure A.1. The mred target structure used in these simulations is shown in figure IV.4. This target structure approximates a modern ultra-thin FDSOI device. The sensitive volume is a 5 nm thick silicon layer. The range cuts in the device structure were set to 500 nm except in the tungsten vias were range cuts were set to 10 nm. Range cuts in the silicon sensitive volume were set to 500 nm and 1 km. Energy deposition due to direct ionization by 56 GeV Fe in the sensitive volume was measured. As can be seen in figure A.1 the long range cuts significantly increases the straggle of the energy deposition distribution. Because the large range cut effectively constrains the energy loss by the Fe ion to one dimension, the path along which the ion travels, the energy deposition distribution takes on the characteristics of the energy loss distribution in that volume. 56 GeV Fe can produce single secondary electrons with MeV of energy. These secondaries have a range larger than the entire target structure and would carry almost all of the energy transferred to them outside of the sensitive volume. With range cuts larger than the secondary's range, however, the secondary is not produced and discretely tracked, and, therefore, the energy transferred to it is deposited in the step in which the event occurred.

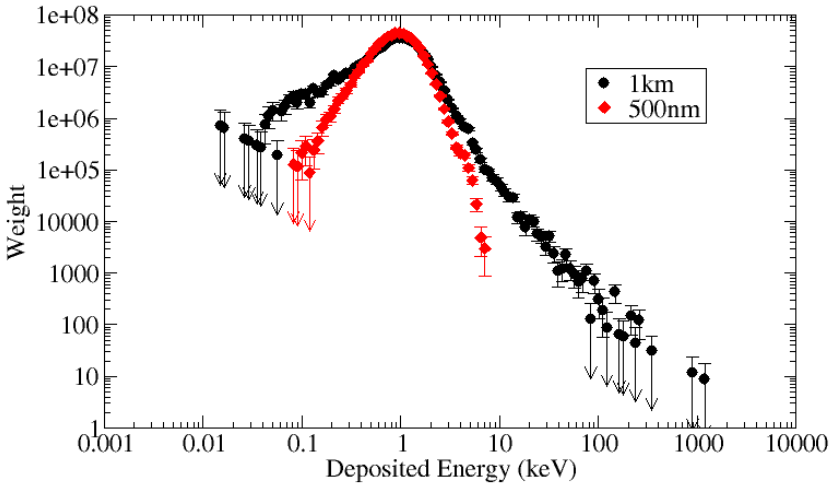

Figure A.1: Differential cross section of energy deposition due to direct ionization from 56 GeV Fe in a 5 nm thick silicon sensitive volume with specified range cuts in the sensitive volume. The mred target structure used in these simulations is shown in figure IV.4 with range cuts outside the sensitive volume set to 500 nm except in the tungsten vias where range cuts are set to 10 nm. The data has been scaled by bin width to give an accurate representation of the underlying energy deposition probability distribution.

This has obvious impacts on SEU simulations, because they require an accurate description of the energy deposited by high energy ions in order to make accurate rate predictions. In general, to accurately simulate energy deposition, range cuts should be on the order of the size of the sensitive volume. This generalization relaxes some as sensitive volumes decrease in size due to GEANT4's use of the continuous slowing down approximation (CSDA) (see II.2) to convert range cuts to energy production cuts for secondary electrons. The CSDA severely overestimates the practical range of low energy secondary electrons, and, therefore, relatively larger cuts may not affect energy deposition in deep submicron sensitive volumes. However, the energy production cut calculated for a specified range cut is material dependent, and, therefore a "large" range cut in one material may be a "small" range cut in another material.

This is an important concept, because modern microelectronic devices contain a large range of materials deposited next to each other in thin films. If range cuts are larger than

the thickness of any one film, the secondary electron environment across several layers of different materials will be affected by the discontinuity in secondary electron energy production cuts at material interfaces. This effect is most pronounced at high-Z/low-Z material interfaces due to the large difference in electron range for a given energy between high-Z and low-Z materials. For instance a range cut of 500 nm in silicon translates to a secondary electron production cut of 256 eV but in tungsten it translates to a secondary electron production cut of 5.4 keV. In a thin tungsten film, a 500 nm range cut suppresses a large number of secondary electrons which would have the energy to travel beyond the film and could travel more than a μm in neighboring silicon. This could be particularly problematic because the probability of an ion generating a secondary electron of given energy is inversely related to the square of the electron energy, and, therefore, accurately modeling the low energy secondary electron environment may be crucial in accurately modeling energy deposition in small volumes.

The importance of understanding how range cuts affect secondary electron production in different materials is illustrated in figure A.2. The mred target structure used in these simulations is shown in figure IV.4 and approximates a modern ultra thin FDSOI device. The sensitive volume is a 5 nm thick silicon film and the contact above it is a 19.23 nm thick tungsten film. As a control the contact material is switched to silicon. The energy deposition in the sensitive volume due to direct ionization by 56 GeV Fe as a function of range cut in the contact material is measured. The range cut in the sensitive volume is set at 500 nm. The dependence of these results on the electron transport code used in the simulation was also explored. The results using PENELOPE 2008 to simulate electron transport are shown in figure A.2a. The results using G4 electrons are shown in figure A.2b.

As can be seen in figure A.2, range cuts in the contact material have an impact on energy deposition in the sensitive volume. Large range cuts in the tungsten contact can even lead to an apparent blocking effect, a reduction in the energy deposition in the sensitive volume due to the tungsten contact, when in reality a tungsten contact has an enhancement effect on the

energy deposition in the sensitive volume. The difference in the energy deposition between the PENELOPE 2008 and GEANT4 electrons is thought to be due to differences in the way the codes handle continuous energy deposition. GEANT4 approximates continuous energy loss by electrons using a CSDA estimate [48]. As has already been stated, this estimate is severely limited in its estimation of energy loss by low energy electrons. Furthermore, a CSDA estimate may not accurately describe energy loss by electrons in small volumes due to increases in energy loss straggling in small volumes. PENELOPE 2008 does not use a continuous energy loss approximation in its simulation of electron transport and, therefore, is expected to be more accurate.

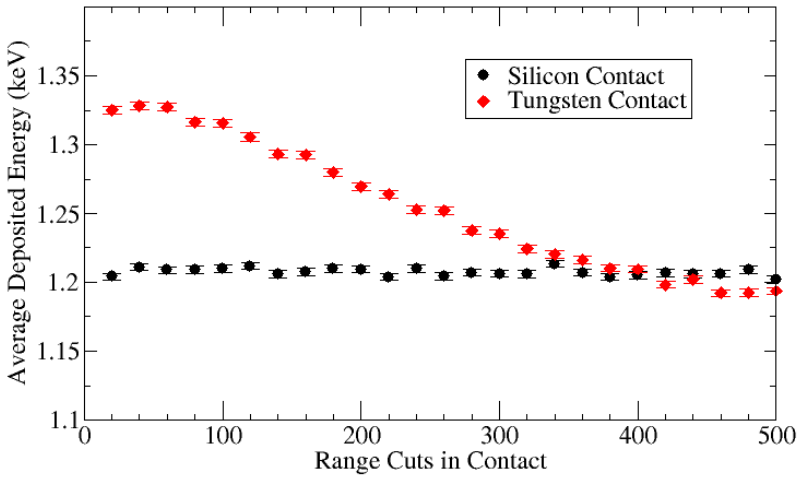

(a) Energy deposition as a function of contact range cuts using PENELOPE 2008

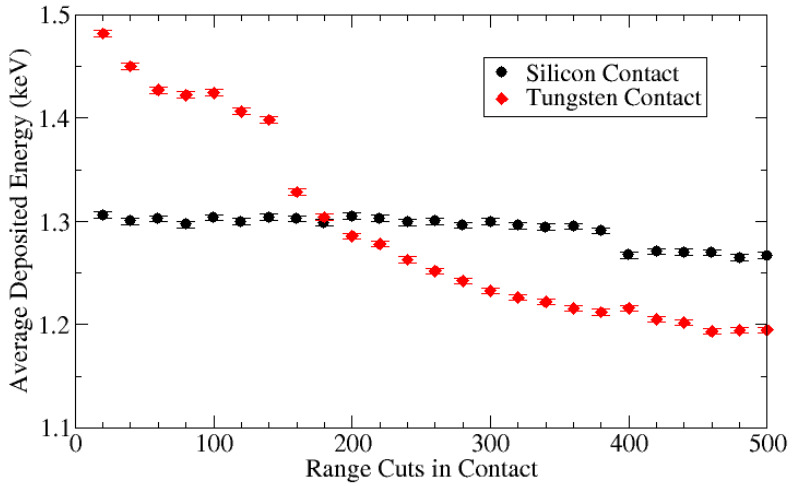

(b) Energy deposition as a function of contact range cuts using EmStandard-Screened

Figure A.2: Effect of range cuts in the contact material on average energy deposition in a neighboring silicon sensitive volume. The mred target structure used in these simulations is shown in figure IV.4. Range cuts in the sensitive volume and the rest of the target structure were set to 500 nm except in the tungsten vias were range cuts were set to 10 nm. In figure A.2a PENELOPE 2008 was used to simulate energy deposition due to electrons. In figure A.2b EmStandardScreened (which uses GEANT4 electrons) was used to simulate energy loss due to ionization.

One thing to be aware of when using low range cuts is an apparent bug in GEANT4 in versions up to at least 9.6. To study the effects of this bug, mred simulations with PENELOPE 2008 were performed using the target structure shown in figure IV.1. This structure consists of a sensitive volume 5 nm thick with 5 µm of material on either side to provide some amount of charge particle equilibrium. Energy deposition in the sensitive volume due to direct ionization by 56 GeV Fe ions was measured. The entire target structure consists of a single material. Range cuts in the layers surrounding the sensitive volume were set at 500 nm with the range cuts in the sensitive volume varying. The results of these simulations are shown in figure A.3. In every material that was tested, average energy deposition due to direct ionization decreased abruptly by approximately twenty five percent when the range cuts in the sensitive were set to a value lower than the mean ionization energy of the material. As the mean ionization energy of a material has no physical meaning, this abrupt change in energy deposition is believed to be a numerical artifact of the Monte Carlo calculations and not physically realistic.

The bug is believed to affect the continuous energy loss portion of the energy deposited due to direct ionization. This is consistent with the observation of the bug with range cuts above the mean ionization energy in the layers surrounding the sensitive volume. It is also consistent with the results seen in figure A.2. When using EmStandardScreened, which uses GEANT4 electrons, a sharp increase in energy deposition in the sensitive volume is observed for both the silicon and tungsten contacts when the range cuts in the contact are below the mean ionization energy of the contact material. This can be seen in figure A.2b. This is believed to be due to an increase in the number of secondary electrons which reach the sensitive volume due to a decrease in the amount of energy they lose from continuous energy losses. These sharp jumps are absent when using PENELOPE 2008 as seen in figure A.2a due to the independence of PENELOPE 2008 electrons from GEANT4 physics. The smoothness of the curves in A.2a further implies that the generation of secondary electrons is not affected by the short range cuts bug.

The effect of the short range cuts bug on the differential cross section for energy deposition is shown in Figure A.4. In this figure, the differential energy deposition distribution for 56 GeV Fe in a 5 nm thick silicon sensitive volume with range cuts just above and just below the mean ionization energy is plotted. The distributions are very similar and it would be difficult to tell from sight that there was something wrong with the simulation. This range cuts issue may be resolved in GEANT4 version 10.

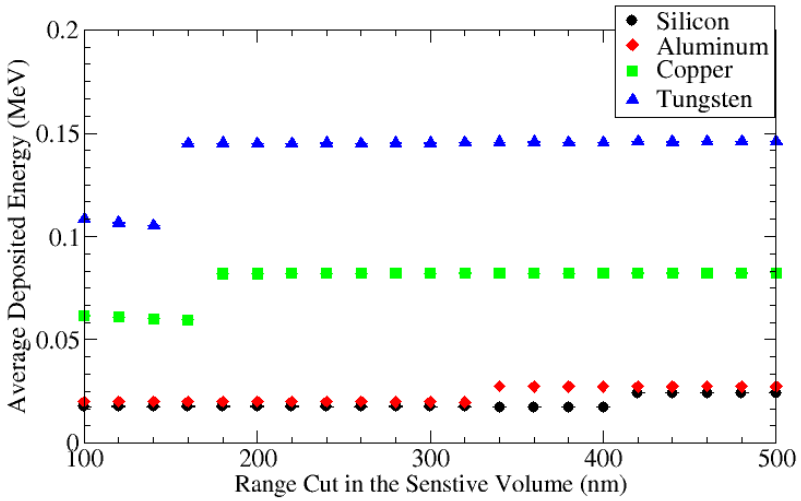

Figure A.3: Effect of range cuts in the sensitive volume on energy deposition due to direct ionization by 56 GeV Fe in a 5 nm thick sensitive volume. The mred target structure used in these simulations is shown in figure IV.1. The target consists of a 5 nm thick sensitive volume with a 5 µm thick layer on both sides of the sensitive volume. The material specifies the material in all layers. Range cuts in the layers surrounding the sensitive volume were set to 500 nm.

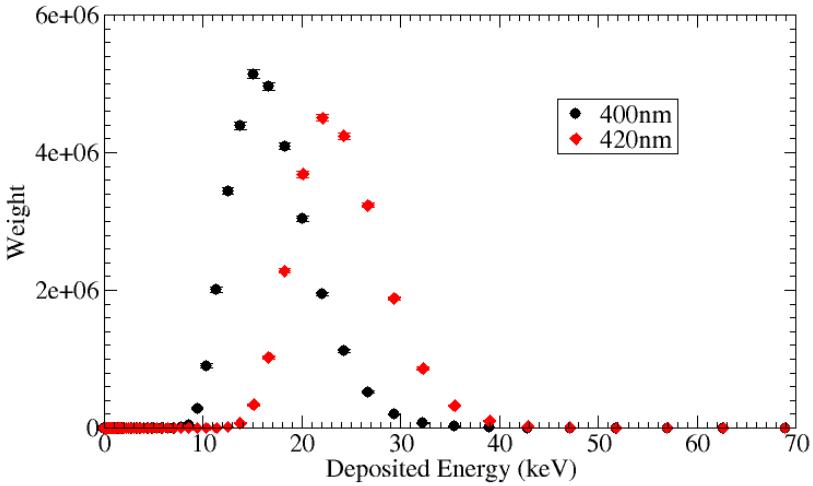

Figure A.4: Dependence of the differential cross section of energy deposition due to direct ionization by 56 GeV Fe in a 5 nm silicon sensitive volume on range cuts in the sensitive volume. The mred target structure used in these simulations is shown in figure IV.1. The target structure consists of a 5 nm thick sensitive volume with 5 µm thick layer on both sides of the sensitive volume. The material in all layers was silicon. Range cuts in the layers surrounding the sensitive volume were set to 500 nm.

A.2 Energy Loss Straggling Limitations

As sensitive volumes shrink in size, the importance of energy deposition straggling increases due to its increased magnitude relative to the average deposited energy. In general, straggle in energy loss and deposition increases for increasing ion energy and decreasing sensitive volume size. However, other factors, such as fluctuations in the charge state of an ion, can greatly affect energy loss straggling. The effect that fluctuations in the charge state of an ion has on energy loss straggling can be seen in figure A.5. This figure shows the enhancement factor for individual ions as plotted together in figure IV.5. The error bar for each point is calculated as $\frac{\mu_w}{\mu_{Si}}\sqrt{(\frac{\sigma_w}{\sqrt{n}})^2+(\frac{\sigma_{Si}}{\sqrt{n}})^2}$ where μ_w and μ_{Si} are the mean energy deposition in the sensitive volume with a tungsten contact and silicon contact respectively. σ_w^2 and σ_{Si}^2 are the variance of the energy deposition distribution of with a tungsten contact and silicon contact respectively and n is the number of ions. For every ion, the number of

ions run at each energy was the same. The error bars, then provide a rough visualization of the variance of the underlying energy deposition distributions.

As can be seen in figure A.5, the variance in the energy deposition distribution for all ions increases with energy except at one point where the variance decreases dramatically. For Fe, this occurs between $250\,\mathrm{MeV\,u^{-1}}$ and $500\,\mathrm{MeV\,u^{-1}}$. For Si this occurs between $100\,\mathrm{MeV\,u^{-1}}$ and $250\,\mathrm{MeV\,u^{-1}}$. For O and C this occurs between $50\,\mathrm{MeV\,u^{-1}}$ and $100\,\mathrm{MeV\,u^{-1}}$. From these numbers, it is apparent that the velocity at which this drop-off in variance of the energy deposition occurs decreases for decreasing ion Z. This is consistent with straggling due to fluctuations in the ion charge state as the velocity at which an ion is fully stripped increases with increasing ion Z.

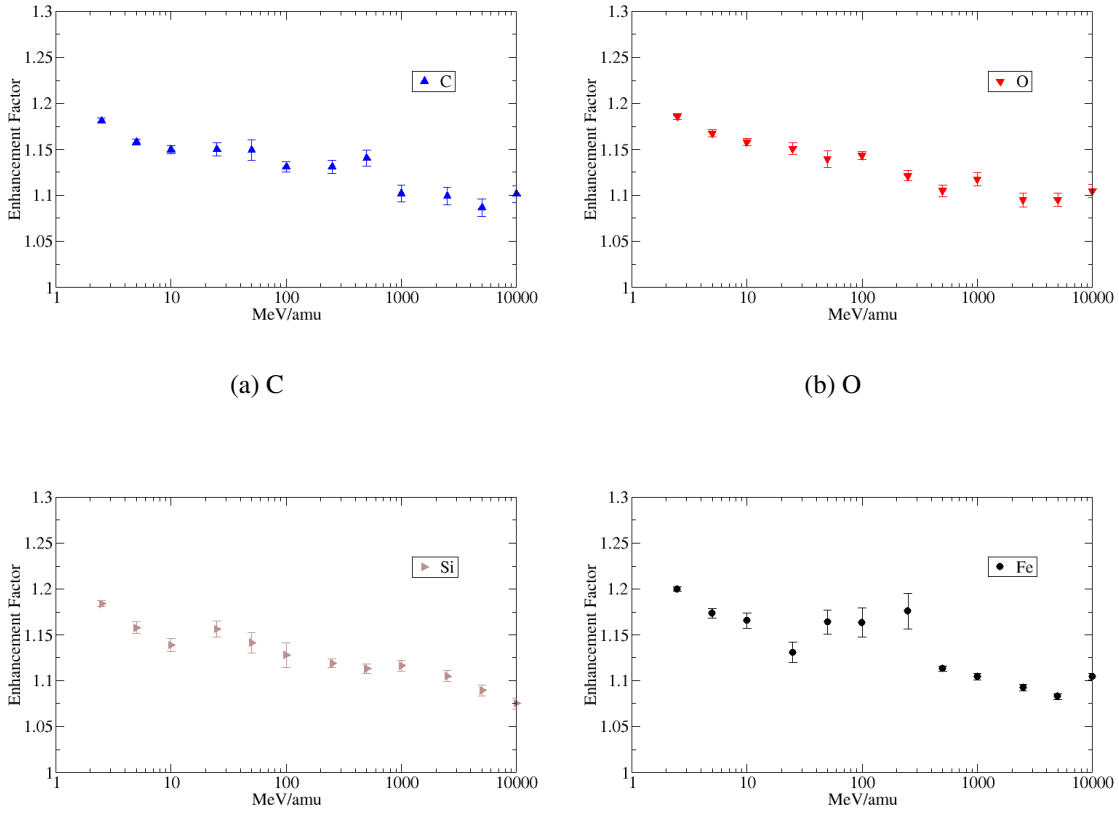

(a) C (b) O

(c) Si (d) Fe

Figure A.5: Enhancement of energy deposition in a 5 nm silicon sensitive volume due to nearby tungsten contact for several ions. The mred target structure used in the simulation is shown in figure IV.4 and approximates a modern ultra-thin body FDSOI device. Estimates in the error are based on the variance of the underlying energy deposition distribution. The total number of ions run for each ion species is the same for all energies although the number of ions run differs for different ion species.

The difference in the energy deposition distributions for 250 MeV u^{-1} and 500 MeV u^{-1} Fe in a 5 nm thick silicon sensitive volume is shown in figure A.6. The differences in the distributions are dramatic, and the accuracy of energy loss straggling for non fully stripped ions should be investigated. Based on the simulations shown in figure A.6, straggling in energy deposition for non-fully stripped heavy ions in small volumes may be extreme. This increases the necessity of correctly simulating energy deposition due to non-fully

stripped ions which unfortunately is difficult due to the complexity of correctly simulating the charge state of non-fully stripped ions. The charge of a non-fully stripped ion is highly dependent on the material through which it is traveling, because the electron density of the material affects electron stripping of the ion. Eventually, an ion travelling through a material reaches an equilibrium charge state which may be fractional due to the tendency of ions to eject and capture electrons as they travel. This equilibrium charge state is used by GEANT4 in energy loss calculations. However, the charge state of an ion is calculated independently for the material it is in. This neglects the effects surrounding material may have on the charge state of an ion as it takes some distance for an ion to reach its equilibrium charge state in a material. As microelectronic device structures contain many thin films comprised of many materials with a wide range of electron densities, it is likely that the charge state of a non-fully stripped ion is affected by multiple materials in the device structure. The impact that this is likely to have on energy deposition is unknown. However, the importance of these charge state fluctuations in the space radiation environments is limited by the fact that low energy ions encountered in the space environment tend to be low Z with heavy ions contained primarily in galactic cosmic rays at energies high enough to be fully stripped.

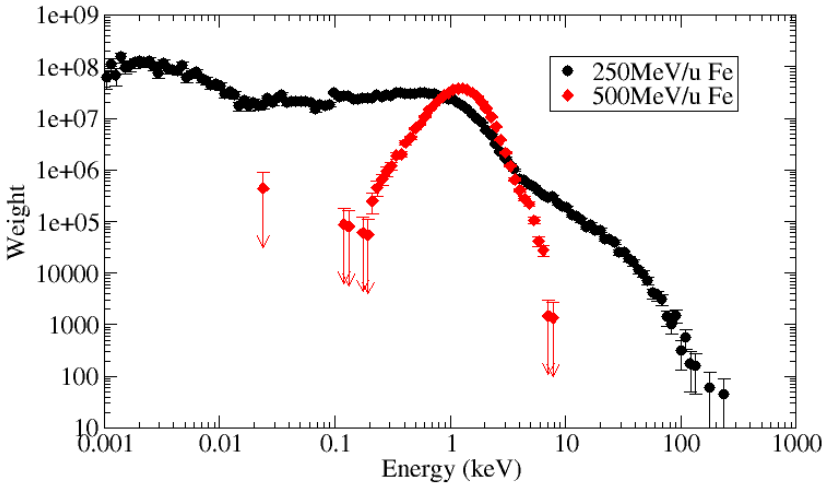

Figure A.6: Differential cross section of energy deposition due to direct ionization in a 5 nm silicon sensitive volume for 250 MeV u^{-1} and 500 MeV u^{-1} Fe. The mred target structure used in these simulations is shown in figure IV.4 and approximates a modern ultra-thin body FDSOI device. The contact material for these simulations was silicon. The data has been scaled by bin width to give an accurate representation of the underlying energy deposition probability distribution.

The accuracy of energy loss straggling calculations for low Z ions in small sensitive volumes is limited by the accuracy of GEANT4 in simulating events which deposit small amounts of energy. To explore energy loss straggling by protons in small volumes, mred simulations with PENELOPE 2008 were performed. The target structure used in these simulations is shown in figure IV.1. This structure consists of a sensitive volume with a 5 µm thick layer on either side to provide some amount of charge particle equilibrium. For these simulations, the entire target structure was silicon. The energy deposition due to direct ionization from 10 MeV protons was measured, and the relative energy deposition straggling was calculated. Relative energy deposition straggling is defined as $\frac{\sigma}{\overline{E}}$ where σ is the standard deviation of the energy loss distribution and $\overline{E}$ is the average of the energy loss distribution. These results were compared to calculations of relative energy loss straggling for 10 MeV protons performed by Akkerman in [10]. The results are shown in figure A.7.

The mred+penelope simulations of relative energy deposition straggling and Akkerman's calculations of relative energy loss straggling are very similar for thick sensitive volumes. As the sensitive volume size decreases, relative energy deposition straggling falls below Akkerman's calculations of relative energy loss straggling. It is unlikely that this discrepancy is due to an absence of charge particle equilibrium as the maximum energy secondary electron that a 10 MeV proton can produce is approximately 20 keV. The range of a 20 keV electron in silicon is approximately 7 µm. As the target is larger than this and the equilibration layer above the sensitive volume is nearly this thick, it is likely that charge particle equilibrium exists in the aggregate. The difference between Akkerman's calculations and mred+penelope's calculations is likely due to inaccuracies in energy deposition events in mred+penelope which deposit less than approximately 500 eV of energy in the sensitive volume as discussed in IV.1. As the sensitive volume depth continues to decrease, there is a sharp decrease in relative energy deposition straggling as calculated by mred+penelope between sensitive volume thicknesses of 2.2 nm and 1.1 nm. This decrease is particularly concerning, because the relative straggling in energy deposition should increase for decreasing sensitive volume depth. The differential energy deposition distribution for 10 MeV protons is in these sensitive volume depths is shown in figure A.8. The decrease in relative energy deposition straggling at 1.1 nm sensitive volume depth is likely due in large part to the appearence of a discontinuity in energy deposition at 10 eV. This is a numerical artifact of the mred+penelope simulations. While these simulations show that mred+penelope in general provides relatively accurate results for energy deposition distribution of light ions in small volumes, they also point to the care that should be taken in basing conclusions solely off of moments of the energy deposition distribution, especially when sensitive volume dimensions drop below 10 nm.

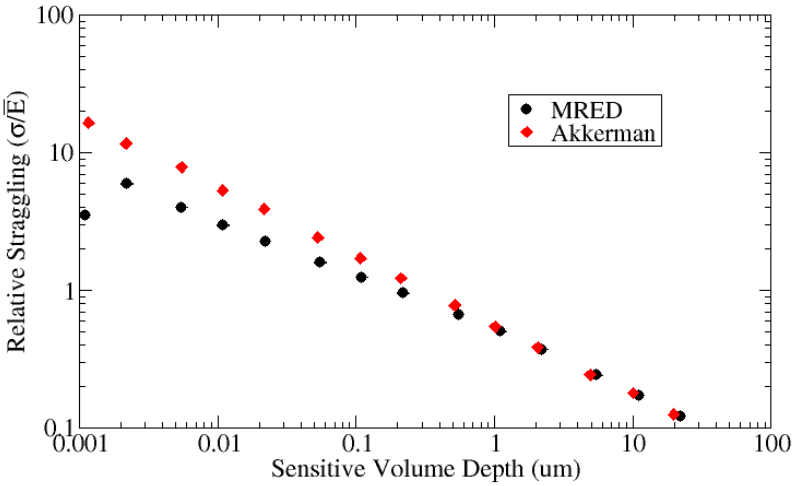

Figure A.7: Relative energy deposition straggling for 10 MeV protons in silicon for sensitive volumes of specified thickness. The mred target structure used in these simulations is shown in figure IV.1 and consists of a sensitive volume with a 5 µm thick layer of silicon on either side of the sensitive volume to provide some amount of charge particle equilibrium. The results are compared to relative energy loss straggling for 10 MeV protons in silicon as calculated by Akkerman in [10].

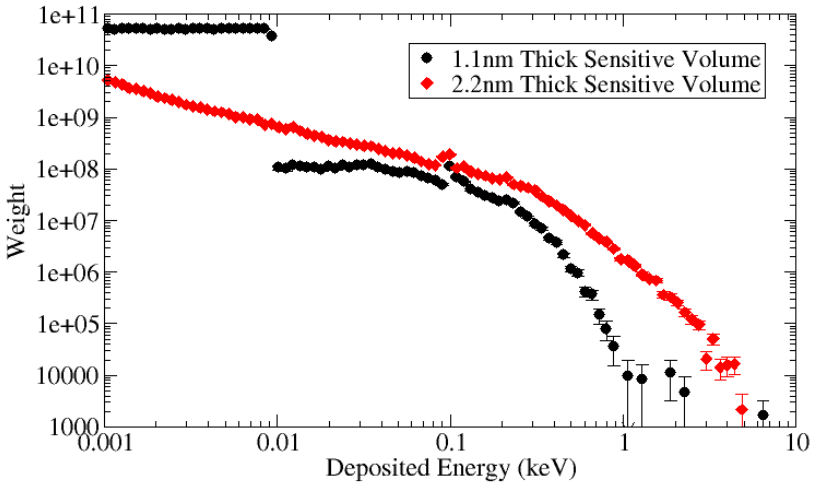

Figure A.8: Differential cross section for energy deposition due to direct ionization from 10 MeV protons in 1.1 nm and 2.2 nm silicon sensitive volumes. The mred target structure used in these simulations is shown in figure IV.1 and consists of a sensitive volume with a 5 µm thick layer of silicon on either side of the sensitive volume to provide some amount of charge particle equilibrium.

BIBLIOGRAPHY

[1] D. Critchlow, "MOSFET scaling–the driver of VLSI technology," *Proc. of the IEEE*, vol. 87, pp. 659–667, Oct. 1999.

[2] S. Bourdarie and M. Xapsos, "The near-earth space radiation environment," *IEEE Trans. Nucl. Sci.*, vol. 55, no. 4, pp. 1810–1832, Aug. 2008.

[3] G. Hellings and K. De Meyer, *High Mobility and Quantum Well Transistors: Design and TCAD Simulation*. Springer, 2013.

[4] A. Akkerman, M. Murat, and J. Barak, "Monte Carlo calculations of electron transport in silicon and related effects for energies of 0.02-200keV," *J. Appl. Phys.*, pp. 113703–1–113703–12, Dec. 2009.

[5] G. F. Knoll, *Radiation Detection and Measurement*. New York: Wiley, 2000.

[6] W. J. Stapor, P. T. McDonald, A. R. Knudson, A. B. Campbell, and B. Glagola, "Charge collection in silicon for ions of different energy but same linear energy transfer (LET)," *IEEE Trans. Nucl. Sci.*, vol. 35, no. 6, pp. 1585–1590, Dec. 1988.

[7] P. E. Dodd, O. Musseau, M. R. Shaneyfelt, F. W. Sexton, C. D'hose, G. L. Hash, R. A. Martinez M., Loemker, J. L. Leray, and P. S. Winokur, "Impact of ion energy on single-event uset," *IEEE Trans. Nucl. Sci.*, vol. 45, no. 6, pp. 2483–2491, Dec. 1998.

[8] M. P. King, R. A. Reed, R. A. Weller, M. H. Mendenhall, R. D. Schrimpf, N. D. Pate, E. A. Auden, and S. L. Weeden-Wright, "Radial characteristics of heavy-ion track structure and implications of delta-ray events for microelectronics," *J. Appl. Phys.*, pp. 053509–1–053509–3, 2012.

[9] M. A. Xapsos, "Applicability of LET to single events in microelectronic structures," *IEEE Trans. Nucl. Sci.*, vol. 36, no. 6, pp. 1613–1621, Dec. 1992.

[10] A. Akkerman and J. Barak, "Ion-track structure and its effects in small size volumes of silicon," *IEEE Trans. Nucl. Sci.*, vol. 49, no. 6, pp. 3022–3031, Dec. 2002.

[11] D. M. Long, D. G. Millward, and J. Wallace, "Dose enhancement effects in semiconductor devices," *IEEE Trans. Nucl. Sci.*, vol. NS-29, no. 6, pp. 1980–1984, Dec. 1982.

[12] J. A. Wall and E. E. Burke, "Gamma dose distributions at and near the interface of different materials," *IEEE Trans. Nucl. Sci.*, vol. 17, no. 6, pp. 305–309, Dec. 1970.

[13] J. L. Barth, C. S. Dryer, and E. G. Stassinopoulous, "Space, atmospheric, and terrestrial radiation environments," *IEEE Trans. Nucl. Sci.*, vol. 50, no. 3, pp. 466–482, Jun. 2003.

[14] E. J. Daly, "Radiation environment evaluation for esa projects," in *AIP Conference Proceedings*, pp. 483–499, 1989.

[15] H. Iwai, "Roadmap for 22nm and beyond (invited paper)," *Microelectronic Engineering*, vol. 86, no. 7-9, pp. 1520–1528, Jul.-Sept. 2009.

[16] E. P. Gusev, D. A. Buchanan, E. Cartier, A. Kumar, D. DiMaria, S. Guha, A. Callegari, S. Zafar, P. Jamison, D. Neumayer, M. Copel, M. Gribelyuk, H. Okorn-Schmidt, C. D'Emic, P. Kozlowski, K. Chan, N. Bajorczuk, L.-A. Pagnarsson, P. Ronsheim, K. Rim, R. J. Flemin, A. Mocuta, and A. Ajmer, "Ultrathin high-K gate stacks for advanced CMOS devices," *Tech. Digest IEDM*, pp. 20.1.1–20.1.4, Dec. 2001.

[17] Y. Yeo, T. King, and C. Hu, "Metal-dielectric band alignment and its implications for metal gate complementary metal-oxide-semiconductor technology," *J. Appl. Physics*, vol. 92, no. 12, pp. 7266–7271, Dec. 2002.

[18] H. L. Hughes and J. M. Benedetto, "Radiation effects and hardening of MOS technology: Devices and circuits," *IEEE Trans. Nucl. Sci.*, vol. 50, no. 3, pp. 500–520, Jun. 2003.

[19] R. Muller, T. I. Kamins, and M. Chan, *Device Electronics for Integrated Circuits*. John Wiley and Sons, 2003.

[20] D. Buchanan, F. McFeely, and J. Yurkas, "Fabrication of midgap metal gates compatible with ultrathin dielectrics," *Appl. Phys. Lett.*, vol. 73, no. 12, pp. 1676–1678, Sept. 1998.

[21] J. Kedzierski, E. J. Nowak, T. Kanarsky, Y. Zhang, D. Boyd, R. Carruthers, C. Cabral, R. Amos, C. Lavoie, R. Roy, J. Newbury, E. Sullivan, J. Benedict, P. Saunders, K. Wong, D. Canaperi, M. Krishnan, K. Lee, B. Rainey, D. Fried, P. Cottrell, H.-S. P. Wong, M. Leong, and W. Haensch, "Metal gate finFET and fully depleted SOI devices using total gate silicidation," *Tech. Digest IEDM*, pp. 247–250, 2002.

[22] H. Shimada, I. Ohshima, T. Ushiki, S. Sugawa, and T. Ohmi, "Tantalum nitride metal gate FD-SOI CMOS FETs using low resistivity self-grown bcc-tantalum layer," *IEEE Trans. Electron Devices*, vol. 48, no. 8, pp. 1619–1626, Aug. 2001.

[23] M. Takahashi, T. Ohno, Y. Sakakibara, and K. Takayama, "Fully depleted 20-nm SOI CMOSFETs with W-clad gate/source/drain layers," *IEEE Trans. Electron Devices*, vol. 48, no. 7, pp. 1380–1385, Jul. 2001.

[24] P. Agnello, "Process requirements for continued scaling of cmos–the need and prospects for atomic-level manipulation," *IBM Journal of Research and Development*, vol. 46, no. 2/3, pp. 317–338, 2002.

[25] D. James, "Intel ivy bridge unveiled – the first commercial tri-gate, high-k, metal-gate, CPU," *Custom Intergrated Circuits Conference*, Sept. 2012.

[26] D. Jacquet, F. Hasbani, P. Flatresse, R. Wilson, F. Arnaud, G. Cesana, T. Di Gilio, C. Lecocq, T. Roy, A. Chhabra, C. Grover, O. Minez, J. Uginet, G. Durieu, C. Adobati, D. Casalotto, F. Nyer, P. Menut, A. Cathelin, I. Vongsavady, and P. Magarshack, "A 3 GHz dual core processor ARM Cortex^{TM}-A9 in 28 nm UTBB FD-SOI CMOS with ultra-wide voltage range and energy efficiency optimization," *IEEE J. Solid-State Circuits*, vol. 49, no. 4, Apr. 2014.

[27] Y. K. Choi, K. Asano, N. Lindert, V. Subramanian, T. J. King, J. Bokor, and H. Chenming, "Ultrathin-body SOI MOSFET for deep-sub-tenth micron era," *IEEE Electron Device Lett.*, vol. 21, no. 5, pp. 254–255, May 2000.

[28] E. J. Nowak, I. Aller, T. Ludwig, K. Kim, R. V. Joshi, C. T. Chuang, K. Bernstein, and R. Puri, "Turning silicon on its edge," *IEEE Circuits and Devices Magazine*, pp. 20–31, Jan-Feb 2004.

[29] P. E. Dodd and L. W. Massengill, "Basic mechanisms and modeling of single-event upset in digital microelectronics," *IEEE Trans. Nucl. Sci.*, vol. 50, no. 3, pp. 593–602, Jun. 2003.

[30] F. McLean and T. Oldham, "Charge funneling in N- and P-type Si substrates," *IEEE Trans. Nucl. Sci.*, vol. 29, no. 6, pp. 2017–2023, Dec. 1982.

[31] J. Schwank, V. Ferlet-Cavroi, M. Shaneyfel, P. Paillet, and P. Dodd, "Radiation effects in SOI technologies," *IEEE Trans. Nucl. Sci.*, vol. 50, no. 3, pp. 522–538, Jun. 2003.

[32] P. M. Lenahan and P. V. Dressendorfer, "Hole traps and trivalent silicon centers in metal/oxide/silicon devices," *J. Appl. Physics*, vol. 55, no. 10, pp. 3495–3499, May. 1984.

[33] H. Barnaby, "Total-ionizing-dose effects in modern CMOS technologies," *IEEE Trans. Nucl. Sci.*, vol. 53, no. 6, Dec. 2006.

[34] J. C. Pickel, "Single-event effects rate prediction," *IEEE Trans. Nucl. Sci.*, vol. 43, no. 2, pp. 483–495, Apr. 1996.

[35] A. J. Tylka, J. H. Adams, P. R. Bober, B. Brownstein, W. F. Dietrich, E. O. Flueckiger, E. L. Petersen, M. A. Shea, D. F. Smart, and E. C. Smith, "CREME96: A revision of the cosmic ray effects on micro-electronics code," *IEEE Trans. Nucl. Sci.*, vol. 44, no. 6, pp. 2150–2160, Dec. 1997.

[36] K. M. Warren, R. A. Weller, M. H. Mendenhall, R. A. Reed, D. R. Ball, C. L. Howe, B. D. Olson, M. L. Alles, L. W. Massengill, R. D. Schrimpf, N. F. Haddad, S. E. Doyle, D. McMorrow, J. S. Melinger, and W. T. Lotshaw, "The contribution of nuclear reactions to heavy ion single event upset cross-section measurements in a high-density seu hardened sram," *IEEE Trans. Nucl. Sci.*, vol. 52, no. 6, pp. 2125–2131, Dec. 2005.

[37] S. Agostinelli, J. Allison, K. Amako, J. Apostolakis, H. Araujo, P. Arce, M. Asai, D. Axen, S. Banerjee, G. Barrand, F. Behner, L. Bellagamba, J. Boudreau, L. Broglia,

A. Brunengo, H. Burkhardt, S. Chauvie, J. Chuma, R. Chytracek, G. Cooperman, G. Cosmo, P. Degtyarenko, A. Dell'Acqua, G. Depaola, D. Dietrich, R. Enami, A. Feliciello, C. Ferguson, H. Fesefeldt, G. Folger, F. Foppiano, A. Forti, S. Garelli, S. Giani, R. Giannitrapani, D. Gibin, J. Gomez Cadenas, I. Gonzalez, G. Garcia Abril, G. Greeniaus, W. Greiner, V. Grichine, A. Grossheim, S. Guatelli, P. Gumplinger, R. Hamatsu, K. Hashimoto, H. Hasui, A. Heikkinen, A. Howard, V. Ivanchenko, A. Johnson, F. Jones, J. Kallenbach, N. Kanaya, M. Kawabata, T. Kodama, R. Kokoulin, M. Kossov, H. Kurashige, a. L. T. Lamanna, E., V. Lara, V. Lefebure, F. Lei, M. Liendl, W. Lockman, F. Longo, S. Magni, M. Maie, E. Medernach, K. Minamimoto, P. Mora de Freitas, Y. Morita, a. N. M. Murakami, K., R. Naratallo, P. Nieminen, a. O. K. a. O. M. a. O. S. Nishimura, T., Y. Oohata, P. K., J. Perl, A. Pfeiffer, T. Sasaki, N. Savvas, a. S. S. Sawada, Y., S. Sei, V. Sirotenko, D. Smith, N. Starkov, H. Stoecker, J. Sulkimo, M. Takahata, S. Tanaka, E. Tcherniaev, E. Safai Tehrani, M. Tropeano, P. Truscott, H. Uno, L. Urban, P. Urban, M. Verderi, A. Walkden, W. Wander, H. Weber, J. P. Wellisch, T. Wanaus, D. C. . Williams, D. Wright, T. Tamada, H. Yoshida, and D. Zschiesche, "G4-a simulation toolkit," *Nucl. Instrum. Methods Physics Res. A*, vol. 506, no. 3, pp. 250–303, 2003.

[38] SWIG Development Team, "Simplified wrapper and interface generator." [online], http://www.swig.org/.

[39] R. A. Weller, M. H. Mendenhall, R. A. Reed, R. D. Schrimpf, K. M. Warren, B. D. Serawski, and L. W. Massengill, "Monte carlo simulation of single event effects," *IEEE Trans. Nucl. Sci.*, vol. 57, no. 4, pp. 1726–1746, Aug. 2010.

[40] F. Salvat, J. Fernandez-Verea, and J. Sempau, "PENELOPE-2008: A code system for Monte Carlo simulation of electron and photon transport." [online], http://www.oecdnea.org/.

[41] R. A. Reed, R. A. Weller, R. D. Schrimpf, M. H. Mendenhall, K. M. Warren, and L. W. Massengill, "Implications of nuclear reactions for single event effects test methods and analysis," *IEEE Trans. Nucl. Sci.*, vol. 53, no. 6, pp. 3356–3362, Dec. 2006.

[42] M. Raine, M. Gaillardin, J. Sauvestre, O. Flament, A. Bournel, and V. Aubry-Fortuna, "Effect of the ion mass and energy on the response of 70-nm SOI transistors to the ion deposited charge by direct ionization," *IEEE Trans. Nucl. Sci.*, vol. 57, no. 4, pp. 1892–1899, Aug. 2010.

[43] R. C. Martin, N. M. Ghoniem, Y. Song, and J. S. Cable, "The size effect of ion charge tracks on single event multiple-bit upset," *IEEE Trans. Nucl. Sci.*, vol. NS-34, no. 6, pp. 1305–1309, Dec.1987.

[44] E. J. Kobetich and R. Katz, "Energy deposition by electron beams and delta rays," *Physical Review*, vol. 170, no. 2, pp. 391–396, Jun. 1968.

[45] F. J. Sigworth and S. M. Sine, "Data transformations for improved display and fitting of single-channel dwel time histograms," *Biophysical Journal*, vol. 52, no. 6, pp. 1047–1054, Dec. 1987.

[46] R. A. Weller, A. L. Sternberg, L. W. Massengill, R. D. Schrimpf, and D. M. Fleetwood, "Evaluating average and atypical response in radiation effects simulations," *IEEE Trans. Nucl. Sci.*, vol. 50, no. 6, pp. 2265–2270, Dec. 2003.

[47] M. P. King, R. A. Reed, R. A. Weller, M. H. Mendenhall, R. D. Schrimpf, B. D. Sierawski, A. L. Sternbert, B. Narasimham, J. K. Wang, E. Pitta, B. Bartz, D. Reed, C. Monzel, R. C. Baumann, X. Deng, J. A. Pellish, M. D. Berg, C. M. Seidleck, E. C. Auden, S. L. Weeden-Wright, N. J. Gaspard, C. X. Zhang, and D. M. Fleetwood, "Electron-induced single-event upsets in static random access memory," *IEEE Trans. Nucl. Sci.*, vol. 60, no. 6, pp. 4122–4129, Dec. 2013.

[48] GEANT4 Collaboration, "Physics reference manual: Version: geant4 9.6.0 (30th november, 2012)." [online], geant4.cern.ch/support/userdocuments.shtml.

[49] A. Dasgupta, D. M. Fleetwood, R. A. Reed, R. A. Weller, M. H. Mendenhall, and B. D. Sierawski, "Dose enhancement and reduction in SiO_2 and high-k MOS insulators," *IEEE Trans. Nucl. Sci.*, vol. 57, no. 6, pp. 3463–3469, Dec. 2010.

[50] A. Dasgupta, D. M. Fleetwood, R. A. Reed, R. A. Weller, and M. H. Mendenhall, "Effects of metal gates and back-end-of-line materials on x-ray dose in HfO_2 gate oxide," *IEEE Trans. Nucl. Sci.*, vol. 58, no. 6, pp. 3139–3144, Dec. 2011.

[51] A. S. Kobayashi, D. R. Ball, K. M. Warren, R. A. Reed, N. Haddad, M. H. Mendenhall, R. D. Schrimpf, and R. A. Weller, "The effect of metallization layers on single event susceptibility," *IEEE Trans. Nucl. Sci.*, vol. 52, no. 6, pp. 2189–2193, Dec. 2005.

[52] P. M. Gouker, B. Tyrrell, M. Renzi, C. Chen, P. Wyatt, J. R. Ahlbin, S. Weeden-Wright, N. M. Atkinson, N. J. Gaspard, B. L. Bhuva, L. W. Massengill, E. Zhang, R. Schrimpf, R. A. Weller, M. P. King, and M. J. Gadlage, "SET characterization in logic circuits fabricated in a 3DIC technology," *IEEE Trans. Nucl. Sci.*, vol. 58, no. 6, pp. 2555–2562, Dec. 2011.

[53] Y. Kimoto, H. Koshiishi, H. Matsumoto, and T. Goka, "Total dose orbital data by dosimeter on board Tsubasa (MDS-1) satellite," *IEEE Trans. Nucl. Sci.*, vol. 50, no. 6, pp. 2301–2306, Dec. 2003.

[54] B. D. Sierawski, J. A. Pellish, R. A. Reed, R. D. Schrimpf, K. M. Warren, R. A. Weller, M. H. Mendenhall, J. D. Black, A. D. Tipton, M. A. Xapsos, R. C. Baumann, X. Deng, M. J. Campola, M. R. Friendlich, H. S. Kim, A. M. Phan, and C. M. Seidleck, "Impact of low-energy proton induced upsets on test methods and rate predictions," *IEEE Trans. Nucl. Sci.*, vol. 56, no. 6, pp. 3085–3092, Dec. 2009.

[55] M. P. King, R. A. Reed, R. A. Weller, M. H. Mendenhall, R. D. Schrimpf, M. L. Alles, E. C. Auden, S. E. Armstrong, and M. Asai, "The impact of delta-rays on single-event upsets in highly scaled SOI SRAMs," *IEEE Trans. Nucl. Sci.*, vol. 57, no. 6, pp. 3169–3175, Dec. 2010.